J. Fluid Mech. (2002), *vol.* 453, *pp.* 201–238.
DOI: 10.1017/S0022112001006887 Printed in the United Kingdom

Large-eddy simulation of the turbulent flow through a heated square duct

By M. SALINAS VÁZQUEZ AND O. MÉTAIS

LEGI-MOST, Institut National Polytechnique de Grenoble, BP 53X,
38041 Grenoble Cédex 9, France

(Received 7 February 2001 and in revised form 29 August 2001)

Large-eddy simulations of a compressible turbulent square duct flow at low Mach number are described. First, we consider the isothermal case with all the walls at the same temperature: good agreement with previous incompressible DNS and LES results is obtained both for the statistical quantities and for the turbulent structures. A heated duct with a higher temperature prescribed at one wall is then considered and the intensity of the heating is varied widely. The increase of the viscosity with temperature in the vicinity of the heated wall turns out to play a major rôle. We observe an amplification of the near-wall secondary flows, a decrease of the turbulent fluctuations in the near-wall region and, conversely, their enhancement in the outer wall region. The increase of the viscous thickness with heating implies a significant augmentation of the size of the characteristic flow structures such as the low- and high-speed streaks, the ejections and the quasi-longitudinal vorticity structures. For strong enough heating, the size limitation imposed by the lateral walls leads to a single low-speed streak located near the duct central plane surrounded by two high-speed streaks on both sides. Violent ejections of slow and hot fluid from the heated wall are observed, linked with the central low-speed streak. A selective statistical sampling of the most violent ejection events reveals that the entrainment of cold fluid, originated from the duct core, at the base of the ejection and its subsequent expansion amplifies the ejection intensity.

1. Introduction

The turbulent flow inside a duct of square or rectangular cross-section is of considerable engineering interest. This flow is characterized by the existence of secondary flows (Prandtl's flow of the second kind) which are driven by the turbulent motion. The secondary flow is a mean flow perpendicular to the main flow direction. It is relatively weak (1–3% of the mean streamwise velocity), but its effect on the transport of heat and momentum is quite significant.

There is still much controversy about the relation between the secondary flow and the ejection mechanism from the wall. Many studies based upon the mean streamwise vorticity equation have shown that this secondary flow is generated by a balance between the secondary Reynolds stress gradients (Demuren & Rodi 1984; Brundet & Baines 1964; Gessner & Jones 1965; Gessner 1983). This generation has been investigated in detail by Huser & Biringen (1993) through a direct numerical simulation (DNS) of a square duct. They have found that the dominant turbulent mechanism is ejections from the wall. The frequency and intensity of these ejections vary significantly with the distance from the duct corner. Close to the corner, the

weak shear inhibits the ejections while, close to the middle of each wall, the strong shear enhances the ejection mechanism. This generates a secondary flow directed from the core of the duct toward the corners and promotes the distortion of the streamwise isolines. This motion yields an anisotropic Reynolds stress distribution.

The aim of the present study is to investigate through large-eddy simulations (LES) the effects of an asymmetric heat flux in the square duct flow. First, our numerical procedure is validated by performing an isothermal duct LES with the four walls at the same temperature and by comparing our results with previous incompressible DNS results by Gavrilakis (1992). A second step is a comparison between the isothermal duct and a heated duct where the temperature of one of the walls is higher than the temperature of the other three walls. Sections 2 and 3 describe the numerical scheme used to discretize the three-dimensional compressible Navier–Stokes equations, the compressible LES formalism and our subgrid-scale model. The following section (§ 4) presents the computational details and defines the main statistical quantities used throughout the paper. Detailed comparisons with previous DNS and LES results for the isothermal duct are presented in § 5. This section also includes a detailed study of the anisotropy of the duct turbulent flow. Finally, §§ 6 and 7 focus on the heated duct dynamics. Several heating intensities are considered and we investigate in detail the modifications of both statistical quantities and three-dimensional flow structures.

2. Governing equations and numerical scheme

2.1. *Governing equations*

In a Cartesian frame of reference, x, y, z, the compressible Navier–Stokes equations can be written in the so-called fast-conservation form, details of which can be found in Ducros, Comte & Lesieur (1996):

$$\frac{\partial \boldsymbol{U}}{\partial t} + \frac{\partial \boldsymbol{F}_i}{\partial x_i} = \boldsymbol{S}. \tag{2.1}$$

$\boldsymbol{U}$ is a five component vector defined by

$$\boldsymbol{U} = {}^T(\rho, \rho u_1, \rho u_2, \rho u_3, \rho e). \tag{2.2}$$

Here $\boldsymbol{u} = (u_1, u_2, u_3)$ is the velocity vector, ρ is the density. In this article, we will also write $\boldsymbol{u} = (u, v, w)$. Equation (2.1) represents the evolution of density (continuity equation), momentum, and total energy defined for an *ideal* gas by

$$\rho e = \rho C_v T + \tfrac{1}{2}\rho(u_1^2 + u_2^2 + u_3^2). \tag{2.3}$$

$\boldsymbol{F}_i$ are fluxes where $\forall i \in \{1, 2, 3\}$, and for a Newtonian fluid are given by

$$\boldsymbol{F}_i = \begin{pmatrix} \rho u_i \\ \rho u_i u_1 + p\delta_{i1} - 2\mu S_{i1} \\ \rho u_i u_2 + p\delta_{i2} - 2\mu S_{i2} \\ \rho u_i u_3 + p\delta_{i3} - 2\mu S_{i3} \\ (\rho e + p)u_i - 2\mu u_j S_{ij} - k\,\partial T/\partial x_i \end{pmatrix}, \tag{2.4}$$

$k = \rho C_p \kappa$ being the thermal conductivity and κ the thermal diffusivity. δ_{ij} is Kronecker's indice and S_{ij} is the deviatoric part of the deformation tensor. Neglecting bulk viscosity, S_{ij} is written

$$S_{ij} = \frac{1}{2}\left(\frac{\partial u_i}{\partial x_j} + \frac{\partial u_j}{\partial x_i} - \frac{2}{3}(\nabla \cdot \boldsymbol{u})\delta_{ij}\right). \tag{2.5}$$

Molecular viscosity is prescribed through the Sutherland empirical law

$$\mu(T) = \mu(T_{ref}) \left(\frac{T}{T_{ref}} \right)^{1/2} \frac{1 + S/T_{ref}}{1 + S/T}, \tag{2.6}$$

where S, T_{ref} and $\mu(T_{ref})$ are functions of the gas. The conductivity $k(T)$ is obtained assuming the molecular Prandtl number is

$$Pr = \frac{\nu}{\kappa} = \frac{C_p \mu(T)}{k(T)}, \tag{2.7}$$

here taken equal to 0.7. The classical equation of state for ideal gas relating the static pressure p, the temperature T and the density ρ,

$$p = R\rho T, \tag{2.8}$$

closes the system, with $R = C_p - C_v$. We recall also that $\gamma = C_p/C_v$ is constant.

For the duct flow, the matrix $\boldsymbol{S}$ in equation (2.1) is given by $\boldsymbol{S} = (0, f(t), 0, 0, U_b f(t))^T$. The uniform body force $f(t)$ which is a function of time has to be introduced in order to impose a constant mass flux in the streamwise direction x. This forcing term appears both in the streamwise momentum equation and in the energy equation. Indeed, to be consistent with the momentum equation, a forcing term $f(t)u_1$ arises in the energy equation. For stability reasons, the local velocity, u_1 is replaced here by the bulk velocity U_b (see §4.2 for a definition). Note that this forcing term is equivalent to the imposition of a mean streamwise pressure gradient and constitutes a convenient and customary way to numerically achieve streamwise homogeneity (see e.g. Coleman, Kim & Moser 1995).

3. Large-eddy simulation

The LES technique consists in trying to deterministically simulate only the large scales of the flow: the small scales are then filtered out, but statistically influence the large-scale motion (see Métais & Lesieur 1996 for details). The LES equations are found by applying a low-pass spatial filter $G_\Delta(\boldsymbol{x})$ of size Δ to the Navier–Stokes equations. This eliminates the scales smaller than the filter size Δ called the sub-grid scales. Mathematically, the filtering operation corresponds to the convolution of any quantity $f(\boldsymbol{x}, t)$ of the flow by the filter function $G_\Delta(\boldsymbol{x})$, in the form

$$\bar{f}(\boldsymbol{x}, t) = \int f(\boldsymbol{y}, t) G_\Delta(\boldsymbol{x} - \boldsymbol{y}) \, \mathrm{d}\boldsymbol{y}, \tag{3.1}$$

and the subgrid-scale field is the departure of the actual flow with respect to the filtered field:

$$f = \bar{f} + f'. \tag{3.2}$$

The compressible LES formalism has been described in detail by Comte & Lesieur (1997).

The application of the filter to the compressible Navier–Stokes equations yields

$$\frac{\partial \bar{\boldsymbol{U}}}{\partial t} + \frac{\partial \bar{\boldsymbol{F}}_1}{\partial x_1} + \frac{\partial \bar{\boldsymbol{F}}_2}{\partial x_2} + \frac{\partial \bar{\boldsymbol{F}}_3}{\partial x_3} = 0, \tag{3.3}$$

with

$$\overline{\rho e} = \overline{\rho \; c_v \; T} + \tfrac{1}{2} \overline{\rho (u_1^2 + u_2^2 + u_3^2)} \tag{3.4}$$

and

$$\bar{p} = \overline{\rho RT}. \tag{3.5}$$

To derive a formalism as close as possible to the incompressible formalism, it is usual in statistical turbulence modelling and in LES to introduce density-weighted or Favre averaging (see Favre 1965). We denote by $\tilde{f}$ the density-weighted filtering of f, defined as

$$\tilde{f} = \frac{\overline{\rho f}}{\bar{f}}. \tag{3.6}$$

We then have

$$\bar{\boldsymbol{U}} = {}^{T}(\bar{\rho}, \bar{\rho}\widetilde{u_1}, \bar{\rho}\widetilde{u_2}, \bar{\rho}\widetilde{u_3}, \bar{\rho}\tilde{e}), \tag{3.7}$$

and the *resolved total energy* is written

$$\overline{\rho e} = \bar{\rho}\tilde{e} = \bar{\rho} C_v \tilde{T} + \tfrac{1}{2}\overline{\rho(u_1^2 + u_2^2 + u_3^2)}. \tag{3.8}$$

The resolved fluxes $\bar{\boldsymbol{F}}_i$ are

$$\bar{\boldsymbol{F}}_i = \begin{pmatrix} \bar{\rho}\tilde{u}_i \\ \overline{\rho u_i u_1} + \bar{p}\delta_{i1} - \overline{2\mu S_{i1}} \\ \overline{\rho u_i u_2} + \bar{p}\delta_{i2} - \overline{2\mu S_{i2}} \\ \overline{\rho u_i u_3} + \bar{p}\delta_{i3} - \overline{2\mu S_{i3}} \\ \overline{(\rho e + p)u_i} - \overline{2\mu S_{ij} u_j} - \overline{k\partial T/\partial x_i} \end{pmatrix}, \tag{3.9}$$

with the filtered equation of state

$$\bar{p} = \bar{\rho} R \tilde{T}. \tag{3.10}$$

We now introduce the usual subgrid-stress tensor $\bar{\mathscr{T}}$ with components

$$\mathscr{T}_{ij} = -\overline{\rho u_i u_j} + \bar{\rho}\tilde{u}_i\tilde{u}_j, \tag{3.11}$$

which we split into its isotropic and deviatoric parts, the latter being denoted $\bar{\tau}$:

$$\mathscr{T}_{ij} = \underbrace{\mathscr{T}_{ij} - \tfrac{1}{3}\mathscr{T}_{ll}\delta_{ij}}_{\tau_{ij}} + \tfrac{1}{3}\mathscr{T}_{ll}\delta_{ij}. \tag{3.12}$$

Equations (3.9) and (3.8) then read

$$\bar{\boldsymbol{F}}_i = \begin{pmatrix} \bar{\rho}\widetilde{u_i} \\ \bar{\rho}\widetilde{u_i}\widetilde{u_1} + (\bar{p} - \tfrac{1}{3}\mathscr{T}_{ll})\delta_{i1} - \tau_{i1} - \overline{2\mu S_{i1}} \\ \bar{\rho}\widetilde{u_i}\widetilde{u_2} + (\bar{p} - \tfrac{1}{3}\mathscr{T}_{ll})\delta_{i2} - \tau_{i2} - \overline{2\mu S_{i2}} \\ \bar{\rho}\widetilde{u_i}\widetilde{u_3} + (\bar{p} - \tfrac{1}{3}\mathscr{T}_{ll})\delta_{i3} - \tau_{i3} - \overline{2\mu S_{i3}} \\ \overline{(\rho e + p)u_i} - \overline{2\mu S_{ij} u_j} - \overline{k\partial T/\partial x_i} \end{pmatrix} \tag{3.13}$$

and

$$\bar{\rho}\tilde{e} = \bar{\rho} C_v \tilde{T} + \tfrac{1}{2}\bar{\rho}(\widetilde{u_1}^2 + \widetilde{u_2}^2 + \widetilde{u_3}^2) - \tfrac{1}{2}\mathscr{T}_{ll}. \tag{3.14}$$

An elegant formulation has been proposed by Comte & Lesieur (1997) through the introduction of a *macro-pressure* and a *macro-temperature*. The *macro-pressure* is defined as

$$\varpi = \bar{p} - \tfrac{1}{3}\mathscr{T}_{ll}. \tag{3.15}$$

and the *macro-temperature*

$$\vartheta = \tilde{T} - \frac{1}{2C_v\bar{\rho}}\mathscr{T}_{ll}. \tag{3.16}$$

The filtered equation of state (3.10) can then be written as

$$\varpi = \bar{\rho}R\vartheta + \frac{3\gamma - 5}{6}\mathscr{T}_{ll}. \tag{3.17}$$

The major advantage of this formulation is that we may derive a closed system of equations in which the unknown trace $\mathscr{T}_{ll}$ of the subgrid-scale tensor no longer explicitly appears. Indeed, it can be shown that the resolved total energy is written

$$\bar{\rho}\tilde{e} = \bar{\rho}C_v\vartheta + \tfrac{1}{2}\bar{\rho}(\widetilde{u_1}^2 + \widetilde{u_2}^2 + \widetilde{u_3}^2). \tag{3.18}$$

Furthermore, for $\gamma = 1.4$, it was shown by Comte & Lesieur (1997) that it is fully justified to neglect the second term of the right-hand side of equation (3.17). We can then write

$$\varpi \simeq \bar{\rho}R\vartheta. \tag{3.19}$$

This makes ϖ computable if $\bar{\rho}$ and ϑ are known.

We next need to introduce the subgrid heat-flux vector, denoted $\boldsymbol{Q}$, with components

$$Q_i = -\overline{(\rho e + p)u_i} + (\bar{\rho}\tilde{e} + \varpi)\tilde{u}_i. \tag{3.20}$$

The exact expression for the filtered fluxes then becomes

$$\bar{\boldsymbol{F}}_i = \begin{pmatrix} \bar{\rho}\widetilde{u_i} \\ \bar{\rho}\widetilde{u_i}\widetilde{u_1} + \varpi\delta_{i1} - \tau_{i1} - \overline{2\mu S_{i1}} \\ \bar{\rho}\widetilde{u_i}\widetilde{u_2} + \varpi\delta_{i2} - \tau_{i2} - \overline{2\mu S_{i2}} \\ \bar{\rho}\widetilde{u_i}\widetilde{u_3} + \varpi\delta_{i3} - \tau_{i3} - \overline{2\mu S_{i3}} \\ (\bar{\rho}\tilde{e} + \varpi)\tilde{u}_i - Q_i - \overline{2\mu S_{ij}u_j} - \overline{k\partial T/\partial x_i} \end{pmatrix}. \tag{3.21}$$

3.1. *Sub-grid model*

The system described above may be closed by making use of the usual variable-density eddy-viscosity and diffusivity models, in the form

$$\tau_{ij} \simeq \bar{\rho}\nu_t\widetilde{S_{ij}}, \tag{3.22}$$

$$Q_i \simeq \bar{\rho}C_p\frac{\nu_t}{Pr_t}\frac{\partial\vartheta}{\partial x_i}. \tag{3.23}$$

The remaining non-computable terms are molecular viscous and diffusive terms, which can be considered of less importance when the Reynolds number is sufficiently large. We therefore simply replace (3.21) by

$$\bar{\boldsymbol{F}}_i \simeq \begin{pmatrix} \bar{\rho}\widetilde{u_i} \\ \bar{\rho}\widetilde{u_i}\widetilde{u_1} + \varpi\delta_{i1} - 2(\bar{\mu} + \bar{\rho}\nu_t)\widetilde{S_{i1}} \\ \bar{\rho}\widetilde{u_i}\widetilde{u_2} + \varpi\delta_{i2} - 2(\bar{\mu} + \bar{\rho}\nu_t)\widetilde{S_{i2}} \\ \bar{\rho}\widetilde{u_i}\widetilde{u_3} + \varpi\delta_{i3} - 2(\bar{\mu} + \bar{\rho}\nu_t)\widetilde{S_{i3}} \\ (\bar{\rho}\tilde{e} + \varpi)\tilde{u}_i - 2(\bar{\mu} + \bar{\rho}\nu_t)\widetilde{S_{ij}}\widetilde{u_j} - [\bar{k} + \bar{\rho}C_p\nu_t/Pr_t]\,\partial\vartheta/\partial x_i \end{pmatrix}, \tag{3.24}$$

in which $\bar{\mu}$ and $\bar{k}$ are linked to ϑ through the Sutherland relation (2.6), a constant molecular Prandtl number $Pr = C_p\bar{\mu}(\vartheta)/\bar{k}(\vartheta) = 0.7$ being assumed. Note that one

of the remarkable aspects of this formulation is that the LES system can be easily deduced from the original compressible Navier–Stokes equations by the following changes:

$$u_i \to \widetilde{u}_i, \quad \rho \to \bar{\rho}, \quad T \to \vartheta, \quad p \to \varpi, \quad e \to \widetilde{e}, \quad \mu \to \bar{\mu} + \bar{\rho} v_t, \quad k \to \bar{k} + \bar{\rho} C_p \frac{v_t}{Pr_t}.$$

This renders the numerical code easily usable both for DNS and for LES without severe modifications.

Expressions for v_t and Pr_t used in the following compressible simulations correspond to the incompressible models described in Métais & Lesieur (1996), the only difference being that here v_t is deduced from the density-weighted filtered velocity field $\tilde{\boldsymbol{u}}$. Our subgrid-scale model is the selective structure function model proposed by David (1993) (see also Métais & Lesieur 1996), the local eddy viscosity, $v_t(\boldsymbol{x}, t)$, is then given by

$$v_t(\boldsymbol{x}, \Delta, t) = C_{ssf} \Delta \sqrt{\widetilde{F}_2(\boldsymbol{x}, \Delta, t)} \tag{3.25}$$

where C_{ssf} can be expressed as a function of the Kolmogorov constant C_K: $C_{ssf} = f(C_K^{-3/2})$ (see David 1993). C_{ssf} takes the value 0.104 for $C_K = 1.4$. Δ is taken equal to $(\Delta x \Delta y \Delta z)^{1/3}$, where Δx, Δy and Δz are the local grid sizes in the three spatial directions.

$\widetilde{F}_2(\boldsymbol{x}, \Delta, t)$ is the second-order velocity stucture function constructed with the field $\tilde{\boldsymbol{u}}$. $\widetilde{F}_2$ is calculated at point $\boldsymbol{x}$ with a local statistical average of square (Favre-filtered) velocity differences between $\boldsymbol{x}$ and the six closest points surrounding $\boldsymbol{x}$ on the computational grid. Interpolation based upon Kolmogorov's 2/3 law for the velocity structure function is used. As proposed by David (1993), the eddy viscosity is switched off when the flow is not three-dimensional enough. The criterion for three-dimensionality is defined as follows: consider at a given time the angle between the vorticity vector at a given grid point and the arithmetic mean of vorticity vectors at the six closest neighbouring points. The eddy viscosity is cancelled at points where this angle is smaller than 20°. Finally, the turbulent Prandtl number is taken equal to 0.6.

3.2. *Equations in generalized coordinates*

The numerical code uses generalized coordinates. The adaptation to generalized coordinates is made by introducing a Jacobian matrix, which transforms a complex geometry in the Cartesian coordinate system (x, y, z), such as a non-uniform grid or a curvilinear geometry, into a simple orthogonal geometry with uniform grid in the generalized coordinate system (ξ_1, ξ_2, ξ_3) where the equations can be more easily solved. For the straight duct, it simply consists in a transformation of a non-uniform grid in the physical space (x, y, z) into a uniform grid in the computational space (ξ_1, ξ_2, ξ_3). Every term in the inverse Jacobian matrix $(\boldsymbol{J}^{-1})$ is expressed as an analytic function of the metrics $\partial x_i / \partial \xi_j$. The metrics are computed and calculated by the first-order internal scheme, then the matrix $(\boldsymbol{J})$ is directly computed from $\boldsymbol{J}^{-1}$ (see Fletcher 1988 for more details).

We can then rewrite the equation (2.1) (or the LES equation (3.3)) as

$$\frac{\partial \hat{\boldsymbol{U}}}{\partial t} + \frac{\partial \hat{\boldsymbol{F}}}{\partial \xi_1} + \frac{\partial \hat{\boldsymbol{G}}}{\partial \xi_2} + \frac{\partial \hat{\boldsymbol{H}}}{\partial \xi_3} = \hat{\boldsymbol{S}} \tag{3.26}$$

with

$$\left.\begin{aligned}
\hat{\boldsymbol{U}} &= \boldsymbol{U}/J, \\
\hat{\boldsymbol{F}} &= \frac{1}{J}\left[\left(\frac{\partial \xi_1}{\partial x_1}\boldsymbol{F}\right) + \left(\frac{\partial \xi_1}{\partial x_2}\boldsymbol{G}\right) + \left(\frac{\partial \xi_1}{\partial x_3}\boldsymbol{H}\right)\right], \\
\hat{\boldsymbol{G}} &= \frac{1}{J}\left[\left(\frac{\partial \xi_2}{\partial x_1}\boldsymbol{F}\right) + \left(\frac{\partial \xi_2}{\partial x_2}\boldsymbol{G}\right) + \left(\frac{\partial \xi_2}{\partial x_3}\boldsymbol{H}\right)\right], \\
\hat{\boldsymbol{H}} &= \frac{1}{J}\left[\left(\frac{\partial \xi_3}{\partial x_1}\boldsymbol{F}\right) + \left(\frac{\partial \xi_3}{\partial x_2}\boldsymbol{G}\right) + \left(\frac{\partial \xi_3}{\partial x_3}\boldsymbol{H}\right)\right], \\
\hat{\boldsymbol{S}} &= \frac{1}{J}\boldsymbol{S}.
\end{aligned}\right\} \tag{3.27}$$

J is the determinant of the matrix $(\boldsymbol{J})$ and $\boldsymbol{U}$ is function of the Cartesian coordinates and time.

3.3. *Numerical scheme*

The system in generalized coordinates is solved by means of an extension of the fully explicit McCormack scheme, second order in time and fourth order in space, devised by Gottlieb & Turkel (1976). Note that we use $\boldsymbol{U}$ in the following formula. It has to be replaced by $\bar{\boldsymbol{U}}$ defined by (3.7) when LES are considered. The numerical scheme is a corrector–predictor scheme defined in one dimension by

predictor

$$U_j^{(1)} = U_j^{(n)} + \tfrac{1}{6}\lambda(-f_{j+2}^{(n)} + 8f_{j+1}^{(n)} - 7f_j^{(n)}) + (\delta t)S_j^{(n)}, \tag{3.28}$$

corrector

$$U_j^{(n+1)} = \tfrac{1}{2}(U_j^{(n)} + (U_j)^{(1)}) + \tfrac{1}{12}\lambda(7f_{j-2}^{(1)} - 8f_{j-1}^{(1)} + f_j^{(1)}) + \tfrac{1}{2}(\delta t)S_j^{(1)}. \tag{3.29}$$

The indices (n), $(n+1)$ and (1) stand respectively for the values of the function at time t, time $t+\delta t$ and at the sub-time-step. Note that the intermediate spatial discretizations are non-centred first-order schemes with a forward-predictor and a backward-corrector. As specified above, the resulting scheme is fourth order in space. The three-dimensional, generalized formulation is written (see Salinas-Vázquez & Métais 1999)

predictor

$$\begin{aligned}
U_{i,j,k}^1 = U_{i,j,k}^n - J_{i,j,k}^P \Bigg[& \frac{\Delta t}{\Delta \xi_1}[\tfrac{7}{6}(\hat{F}_{i+1,j,k}^n - \hat{F}_{i,j,k}^n) - \tfrac{1}{6}(\hat{F}_{i+2,j,k}^n - \hat{F}_{i+1,j,k}^n)] \\
& + \frac{\Delta t}{\Delta \xi_2}[\tfrac{7}{6}(\hat{G}_{i+1,j,k}^n - \hat{G}_{i,j,k}^n) - \tfrac{1}{6}(\hat{G}_{i+2,j,k}^n - \hat{G}_{i+1,j,k}^n)] \\
& + \frac{\Delta t}{\Delta \xi_3}[\tfrac{7}{6}(\hat{G}_{i+1,j,k}^n - \hat{G}_{i,j,k}^n) - \tfrac{1}{6}(\hat{G}_{i+2,j,k}^n - \hat{G}_{i+1,j,k}^n)]\Bigg]
\end{aligned} \tag{3.30}$$

corrector

$$\begin{aligned}
U_{i,j,k}^{n+1} = \tfrac{1}{2}[U_{i,j,k}^1 + U_{i,j,k}^n] - \tfrac{1}{2}J_{i,j,k}^C \Bigg[& \frac{\Delta t}{\Delta \xi_1}[\tfrac{7}{6}(\hat{F}_{i,j,k}^1 - \hat{F}_{i-1,j,k}^1) - \tfrac{1}{6}(\hat{F}_{i-1,j,k}^1 - \hat{F}_{i-2,j,k}^1)] \\
& + \frac{\Delta t}{\Delta \xi_2}[\tfrac{7}{6}(\hat{G}_{i,j,k}^1 - \hat{G}_{i-1,j,k}^1) - \tfrac{1}{6}(\hat{G}_{i-1,j,k}^1 - \hat{G}_{i-2,j,k}^1)] \\
& + \frac{\Delta t}{\Delta \xi_3}[\tfrac{7}{6}(\hat{G}_{i,j,k}^1 - \hat{G}_{i-1,j,k}^1) - \tfrac{1}{6}(\hat{G}_{i-1,j,k}^1 - \hat{G}_{i-2,j,k}^1)]\Bigg]
\end{aligned} \tag{3.31}$$

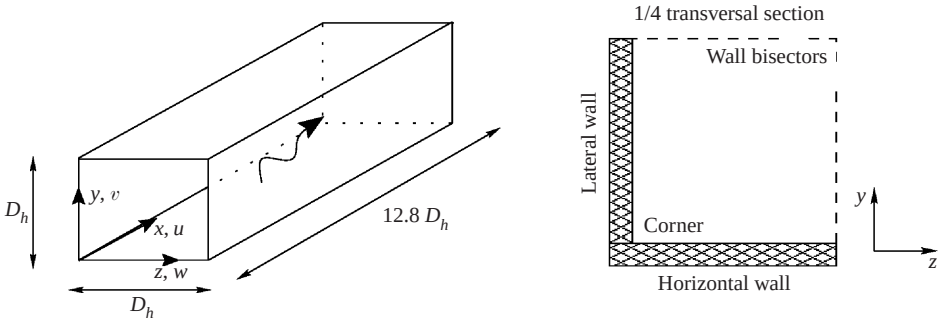

FIGURE 1. Sketch of the computational domain.

J^C and J^P are the determinants of the Jacobian matrix computed with the forward and backward schemes.

4. Flow configuration and computational details

4.1. *Initial and boundary conditions*

The initial conditions for the mean velocity field of the isothermal duct consist in two superimposed laminar Poiseuille profiles respectively sheared along the y- and the z-directions (see figure 1 for the definition of the coordinate axes). At each point, the minimal value of the two profiles is taken. A uniform pressure is prescribed and the temperature distribution is derived from the velocity distribution from the so-called Crocco–Busemann relation (see Schlichting 1979). A white noise of amplitude $A \approx 5\% U_b$ is superimposed on the mean velocity. The statistically converged state of the isothermal duct is used as the initial condition for the heated duct.

The boundary conditions at the walls are no-slip, isothermal: these are compatible with the use of periodic boundary conditions along the streamwise direction x. The wall pressure is obtained by solving the Navier–Stokes equations at the wall. In the heated case, we will call respectively the *horizontal wall* and the *lateral wall* the wall parallel to the z-direction (corresponding to $y = 0$) and the wall parallel to the y-direction (corresponding to $z = 0$). Note that this is an arbitrary definition since gravity effects are found to be negligible (see § 4.3). When heating is applied, a temperature T_h is imposed at the horizontal wall which is higher than the temperature of the other three walls. The latter have an identical reference temperature denoted T_w. Three different cases are studied corresponding respectively to $T_h/T_w = 1.75$, 2.5 and 3.25.

4.2. *Definition of statistical quantities*

Mean quantities We take advantage of the periodicity in the x flow direction and the statistical flow stationarity to define the mean quantities as the averaging in the homogeneous direction, x, and in time. For any given quantity $f(\boldsymbol{x}, t)$, the mean f will be written as $\langle f \rangle(y, z)$, y and z being the transverse directions of the computational domain. The fluctuation $f'(\boldsymbol{x}, t)$ from the mean satisfies $f'(\boldsymbol{x}, t) = f(\boldsymbol{x}, t) - \langle f \rangle(y, z)$. Note that here we use the conventional notation with a prime but the fluctuation is obviously distinct from the subgrid-scale field previously defined by equation (3.2). For convenience, we denote $U(y, z) = \langle u \rangle(y, z)$ and $W(y, z) = \langle w \rangle(u, z)$.

Bulk quantities The bulk quantity f_b refers to the quantity $\langle f \rangle(y, z)$ averaged along

the y- and z-directions, so that

$$f_b = \frac{1}{LyLz}\int_0^{Lz}\int_0^{Ly}\langle f\rangle(y,z)\,\mathrm{d}y\,\mathrm{d}z. \tag{4.1}$$

Ly and Lz are the transverse dimensions of the computational domain. The bulk velocity U_b involves the density and is defined as

$$U_b = \frac{[\rho u]_b}{\rho_b} \tag{4.2}$$

where ρ_b is the bulk density.

Wall units $\tau(y,z)$ is the wall shear stress based upon the mean viscosity and upon the normal derivative of the mean longitudinal velocity component U, both quantities taken at the wall:

$$\tau(y,z) = \left[\langle\mu\rangle\frac{\partial U}{\partial n}\right]_w, \tag{4.3}$$

where n designates the direction normal to the wall. We call τ the *local* wall shear stress. A more *global* quantity can be obtained by averaging on the walls: τ^a stands for the averaged value of τ over the four walls of the duct in the non-heated case. In the heated case, since we focus upon the flow behaviour near the heated wall, τ^a designates the averaged value over the heated wall only. From both local and global variables τ and τ^a, we may construct local and global friction velocities, respectively called u_τ^l and u_τ:

$$u_\tau^l(y,z) = \sqrt{\frac{\tau}{\langle\rho\rangle}}, \tag{4.4}$$

$$u_\tau(y,z) = \sqrt{\frac{\tau^a}{\langle\rho\rangle}}. \tag{4.5}$$

Similarly, the local and the global viscous thicknesses are

$$\delta^l(y,z) = \frac{\langle\mu\rangle}{\langle\rho\rangle u_\tau^l}, \tag{4.6}$$

$$\delta(y,z) = \frac{\langle\mu\rangle}{\langle\rho\rangle u_\tau}. \tag{4.7}$$

We finally define a viscous thickness δ^a and a friction velocity u_τ^a which do not depend on the position by averaging $\delta^l(y,z)$ and $u_\tau^l(y,z)$, respectively, on the four walls of the duct in the non-heated case and on the heated wall in the case with heating.

4.3. *Computation details*

The size of the computational domain is taken equal to $12.8D_h \times D_h \times D_h$ (D_h being the hydraulic diameter), in the x (streamwise), y and z (transverse) directions respectively. For the most strongly heated case (see § 6), corresponding to $T_h/T_w = 3.25$, a larger streamwise dimension of $18D_h$ is used. Figure 2 shows samples of two-point correlations of velocity fluctuations for the isothermal and the heated duct corresponding to $T_h/T_w = 2.50$. These are representative of the streamwise length of the longest turbulence structures present within the flow. Both for the non-heated and for the heated cases, the correlation coefficient is close to zero for $x/D_h = 6.4$. Therefore, a computational domain of streamwise length $12.8D_h$ is considered to be sufficient. However, figure 2 shows that this length tends to be longer when

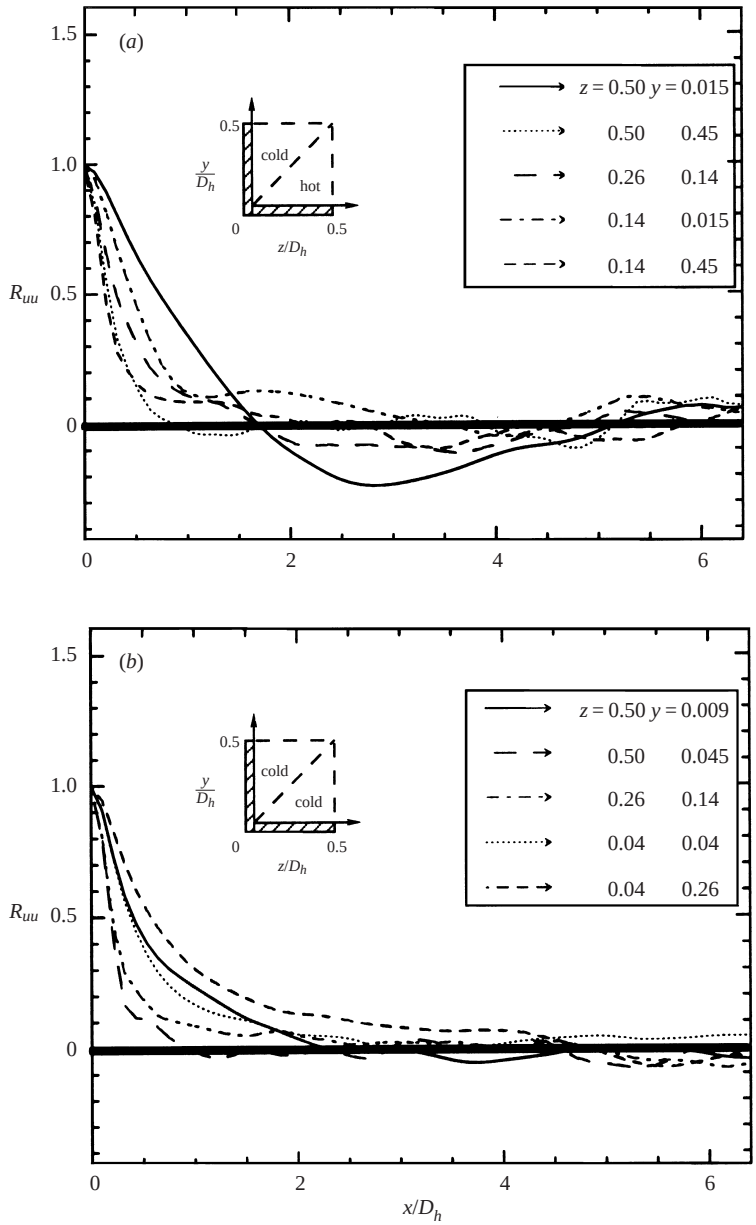

FIGURE 2. Streamwise two-point correlations, R_{uu}, of the streamwise velocity component at different locations. (*a*) Heated square duct and (*b*) isothermal square duct.

heating is applied: we therefore increase it to $18D_h$ for $T_h/T_w = 3.25$. We recall that statistical quantities, those between brackets $\langle\,\rangle$, are obtained by averaging the flow in the homogeneous direction, x, and in time. The quantities obtained with such an averaging procedure will be referred to as mean quantities.

For all the computations, the computational grid consists of $120 \times 60 \times 60$ nodes along x, y and z. In order to correctly simulate the near-wall regions, a non-uniform (orthogonal) grid with a hyperbolic-tangent stretching (see Le, Moin & Kim 1997) is used in the y- and z-directions. The distribution of the discretization points is

identical in the y- and z-directions. The wall units are *a priori* determined through the friction velocity obtained by the Jones equation (Jones 1976):

$$\frac{1}{f_D^{1/2}} = 2\log(Re_i f_D^{1/2}) - 0.8, \tag{4.8}$$

where f_D is D'Arcy's factor and $Re_i = 1.125 Re_b$ ($f_D = 8(u_\tau/U_b)^2$). For the isothermal computation, the minimal and the maximal grid spacings in the y- and z-directions are respectively 1.0 and 12 wall units. The grid spacing in the x-direction is $\Delta x^+ = 42$ for the two cases.

The isothermal LES is performed at a Reynolds number of $Re_\tau = 393$ based upon the friction velocity and the hydraulic diameter. This corresponds to a Reynolds number $Re_b = 6000$ based on the bulk velocity. The two previous Reynolds numbers, Re_τ and Re_b, are defined with the bulk density from (4.2) and the dynamic viscosity at the wall temperature. The Mach number M based upon the bulk velocity and the wall temperature is taken equal to 0.5. The compressibility effects are then expected to be small in the isothermal case. For the heated duct simulations, the bulk Reynolds number and the Mach number are identical to the non-heated case with $Re_b = 6000$ and $M = 0.5$ (based upon the bulk velocity and the temperature of the non-heated walls T_w). It is well known that the compressible Navier–Stokes equations at low Mach number become very stiff because of the large difference in magnitude between the acoustic and dynamic velocities. The choice of the time step is governed by the speed of the sound waves, making the computation extremely time consuming. As a consequence, relatively low resolutions have to be utilized to allow computations in reasonable computing time. Thus, LES must be used if we wish to study relatively high Reynolds number flows.

As shown in previous studies (see Wardana, Ueda & Mizomoto 1994), if the non-dimensional number $Gr/Re^2 \ll 1$ (Gr is the Grashof number), the buoyancy effects are negligible. In the present simulations, we have not introduced any buoyancy forcing since $(Gr/Re^2)_b \approx O(10^{-7})$. The index b denotes bulk quantities (see (4.1)).

5. The isothermal duct

To validate our numerical procedure and subgrid-scale models, we first present comparisons with the incompressible square duct DNS by Gavrilakis (1992) ($Re_\tau = 300$, $Re_b = 4410$) and by Huser & Biringen (1993) ($Re_\tau = 600$, $Re_b = 10\,320$). We have checked that, in our low-Mach number LES, the compressibility effects are weak: the maximal mean velocity divergence is indeed of the order of $10^{-3}(U_b/D_h)$. This makes the comparison significant.

We first have to choose the optimal grid resolution, which has to be determined as a compromise between the quality of the results and affordable computer time. Figure 3 compares, for the isothermal duct, the results of a computation at a resolution of $120 \times 60 \times 60$ discretization points and of a computation at a lower resolution consisting of $64 \times 50 \times 50$ discretization points. For this latter case, the minimal and maximal distances in the directions normal to the walls are 1.8 and 15 wall units respectively. The grid spacing in the longitudinal direction is $\Delta x^+ = 78$. To increase the statistical sampling, flow symmetries are eventually utilized. Some of the distributions are then ensemble averaged over the eight similar triangles formed by the wall and the diagonals of the isothermal square duct. The flow statistics are collected over 90 time units (D_h/U_b) for high-resolution simulations.

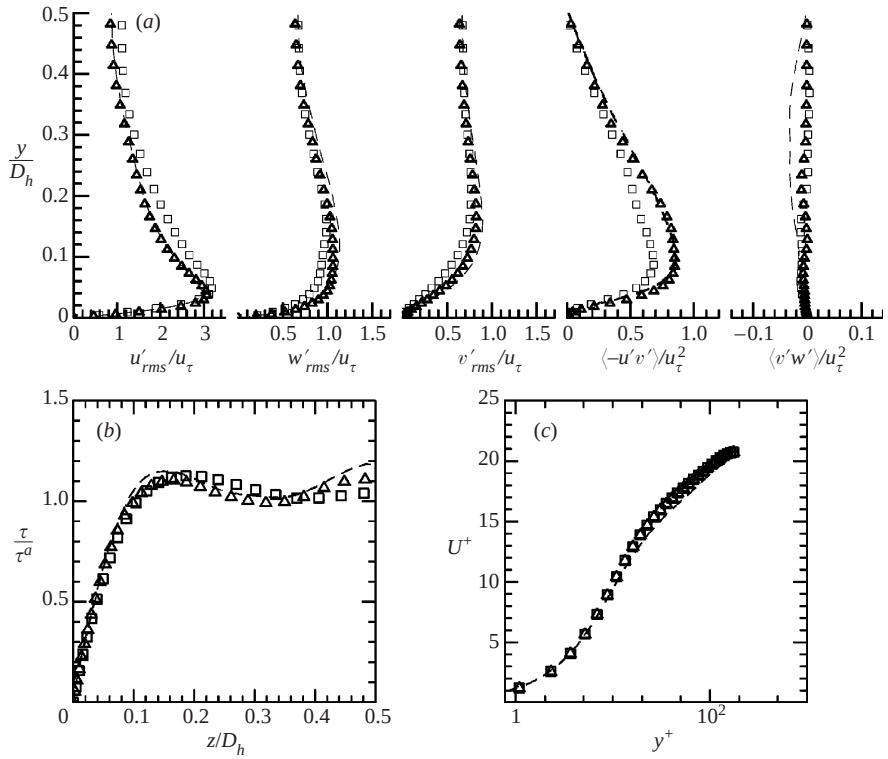

FIGURE 3. Isothermal duct. Comparison of Gavrilakis' (1992) DNS with our LES at different resolutions: — —, Gavrilakis's DNS; □, low resolution LES; △, high resolution LES. (*a*) Profiles of the r.m.s. of the three velocity components and profiles of the Reynolds stress components normalized by the friction velocity ($u_\tau(y,z)$, see (4.5)) at the wall bisector. (*b*,*c*) Local wall shear stress (τ) normalized by the averaged wall shear stress (τ^a) as a function of the distance from the lateral wall z and mean streamwise velocity at the wall bisector (U) normalized by the friction velocity $u_\tau(y,z)$.

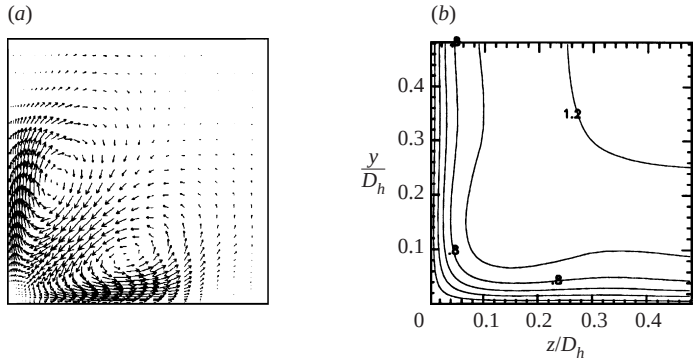

FIGURE 4. Isothermal duct: (*a*) secondary mean flow vectors; (*b*) iso-contours of the mean streamwise velocity (normalized by the bulk velocity U_b).

Figure 3 shows that the statistical quantities based both upon the velocity fluctuations and the mean quantities are considerably improved when the resolution is increased: a very good agreement with Gavrilakis' DNS results is indeed obtained.

We now concentrate on the higher resolution computations. The contours of the

	Gavrilakis (1992)	LES
U_0/U_b	1.33	1.29
Max (τ/τ^a)	1.18	1.11
Max (W/U_b)	1.9%	1.92%
u_τ^a/U_b (% error)	0.0655 (Jones 1976)	0.06201 ($\approx$ 5.32%)

TABLE 1. Comparison of statistical results.

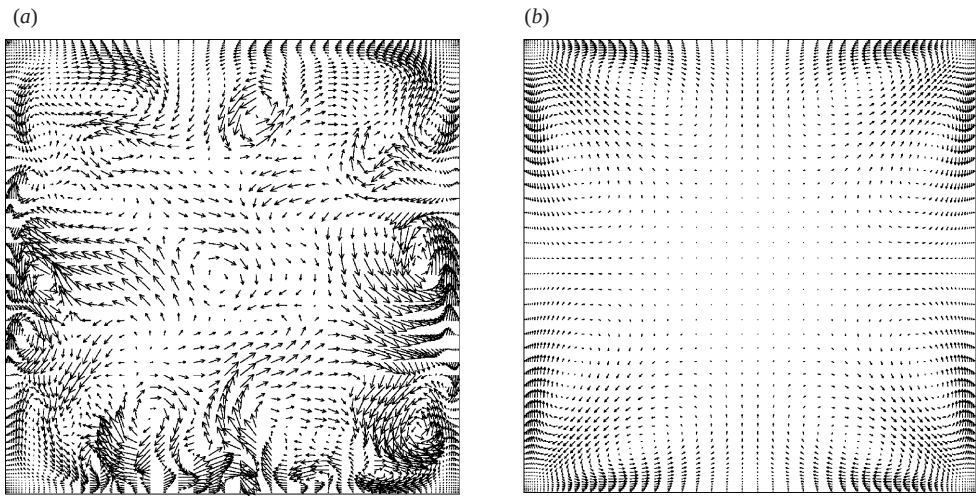

FIGURE 5. Isothermal duct, secondary flow vectors: (*a*) instantaneous secondary flow vectors; (*b*) mean secondary flow vectors. The vector size is function of the secondary flow magnitude.

mean streamwise velocity and the mean secondary flow vectors in a quarter of a cross-section are shown in figure 4. The mean streamwise velocity is directed away from us. The mean secondary flow vectors reveal the existence of two streamwise counter-rotating vortices in each corner of the duct. The velocity maximum associated with this flow is around 1–2% of the bulk velocity, $W_{max}/U_b = 1.192\%$. The distribution of the streamwise velocity contours in the vicinity of the corner is due to the momentum transfer by the secondary flows from the core of the duct toward the corner, Huser & Biringen (1993). One interesting characteristic of this transverse flow is the drastic difference in magnitude between the mean and the instantaneous secondary flow fields. The instantaneous transverse flow field in a whole section is shown in figure 5. It clearly indicates a very pronounced flow variability with an instantaneous field very distinct from the mean field. The maximum intensity of the transverse fluctuating velocity field is of the order of ten times the maximum of the corresponding mean velocity field. For the vorticity, the transverse motions are associated with streamwise vorticity generation, whose maximum is about one third of the transverse vorticity maximum.

Figure 6(*a*) clearly demonstrates (see also Salinas-Vázquez & Métais 1999) that the local wall shear stress (τ/τ^a) distribution at the wall is very sensitive to the numerical resolution. This quantity therefore constitutes a very good quality check for any computation. The wall shear stress is normalized here by its spatially averaged value obtained through integration over the whole length of the four walls of the duct

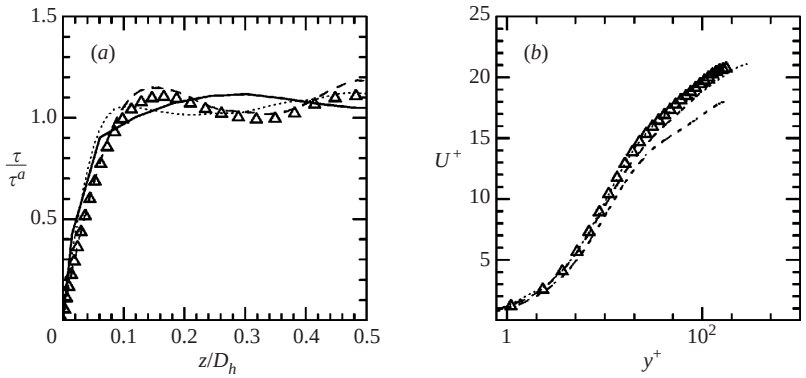

FIGURE 6. Isothermal duct. Comparison between the results of the present LES (△), Knight & Patel (1985) (———), DNS Gavrilakis (1992) (— —), DNS Huser & Biringen (1993) (· · · · · ·) and 'log-law' (— - —). (*a*) Local wall shear stress (τ), normalized by the averaged wall shear stress (τ^a) and (*b*) mean streamwise velocity at the wall bisector (U), normalized by the friction velocity ($u_\tau(y,z)$).

(τ^a). Although the Reynolds numbers are slightly different, Gavrilakis' DNS and the present LES compares very well. The local wall shear stress exhibits two local maxima located around $z/D_h = 0.2$ and $z/D_h = 0.5$. Gavrilakis' DNS results exhibit just one maximum located around $z/D_h = 0.5$. The values of these maxima are slightly lower than those given by Gavrilakis (1992), especially at the duct centre. However, the DNS by Huser & Biringen (1993) performed at higher Reynolds number show a decrease with increasing Reynolds number (see figure 6). The normalized mean velocity profile at the wall bisector (middle plane of the duct) as a function of the distance from the wall is compared with Gavrilakis' and Huser & Biringen's data and a good agreement is obtained (figure 6). Compared with the classical plane channel or boundary layer, the 'log law' is slightly shifted upward with a smaller value of Kármán's constant (see Gavrilakis 1992). Note that the profile is normalized here by the friction velocity, $u_\tau(y,z)$, defined by (4.5). It can be checked that a normalization by the *local* friction velocity, $u_\tau^l(y,z)$ (see (4.4)), moves the profiles closer to the classical 'log law'.

Table 1 shows various quantities related to the mean flow. Our LES give $U_0/U_b \approx 1.29$ where U_0 is the value of the mean velocity at the duct centreline. It is consistent with the values obtained by Gavrilakis (1992) of 1.33 and by Demuren & Rodi (1984) of 1.25. Note that u_τ/U_b is 5.3% smaller than that obtained through Jones' correlation (Jones 1976).

In figure 7, the profiles of the normalized streamwise and transverse mean velocity profiles $U(y,z)/U_b$ and $W(y,z)/U_b$ are plotted at different constant-z planes and are compared with those obtained by Gavrilakis (1992). The $W(y,z)$ profiles clearly indicate the presence of the secondary flows. Their location and their magnitude are very well reproduced by our LES. Note that the mean secondary flow is relatively weak (1–2% of the bulk streamwise velocity), but its effect on the transport of heat and momentum is quite significant. If one wishes to correctly reproduce this weak secondary flow with a classical one-point-closure statistical modelling approach, elaborate second-order models have to be employed. It is important to note that LES without any modification of the model constants are able to correctly reproduce such statistical quantities.

The LES and DNS turbulent intensity profiles are also compared in figure 7 for five different constant-z planes, $z/D_h = 0.05$, 0.15, 0.25, 0.35 and 0.5 (for convenience, we use these values; however they correspond to a distance of $z/D_h = 0.053$, 0.147,

0.261, 0.349, 0.483 for our LES and $z/D_h = 0.052$, 0.149, 0.258, 0.345, 0.485 for Gavrilakis' DNS). The intensities are normalized by the friction velocity, $u_\tau(y,z)$. The discrepancies mainly affect the $\langle v'w' \rangle$ component of the Reynolds stress tensor with a maximum discrepancy of about 10%. The agreement is otherwise very satisfactory. In the middle plane ($z/D_h = 0.5$), a strong turbulent activity is observed: the r.m.s. velocity-fluctuation profiles exhibit trends which are very similar to standard turbulent channel flows or boundary layers. Indeed, the u'_{rms} component dominates the other two components with a very marked peak close to the wall. The spanwise velocity r.m.s. w'_{rms} is slightly larger than the normal velocity r.m.s. v'_{rms}. In the vicinity of the wall, all r.m.s. values decrease when we approach the corner and a very low level of turbulent activity is reached. The Reynolds stress component $\langle -u'v' \rangle$ constitutes the signature of ejections from the wall and sweeping motion towards the wall. In the middle plane, its peak is further from the wall than the u'_{rms} peak and its profile resembles the classical profile observed in turbulent channel flow. The $\langle -u'v' \rangle$ peak becomes smaller and smaller as we approach the corner: this indicates that ejections and sweeps are almost totally absent in the corner region. This is consistent with figure 6 which shows that the local wall shear stress associated with the longitudinal mean velocity is strong in the duct middle plane, promoting ejections and sweeps, while a weaker shear is observed near the corner which is less favourable for these motions. Ejections and sweeps will be investigated in greater detail in § 7.3. Due to the presence of the lateral wall, the mean Reynolds stress has three non-zero components $\langle u'v' \rangle$, $\langle u'w' \rangle$ and $\langle v'w' \rangle$. This is at variance with the classical boundary layer for which periodicity is assumed in the spanwise direction so that $\langle u'v' \rangle$ is the only non-zero component. As pointed out by previous authors (see Huser & Biringen 1993), $\langle v'w' \rangle$ is closely related to the presence of secondary flow. Indeed the secondary flow generation is often attributed to the strong near-wall gradients (normal and lateral gradients) of $\langle v'w' \rangle$ as well as to the strong gradients of $\langle w'^2 \rangle$ and $\langle v'^2 \rangle$ created between the wall bisector and corner (see Demuren & Rodi 1984). It is important to note that all the statistical quantities are very well reproduced by the LES although these are performed at considerably less cost than the DNS. Indeed, the present LES utilized a grid resolution ≈ 7.6 times coarser than the resolution used in Gavrilakis' DNS.

A more detailed analysis of the flow anisotropy may be performed through the anisotropy-invariant map proposed by Lumley & Newman (1977). This map characterizes the various possible states of the turbulence from the anisotropy tensor b_{ij} deduced from the Reynolds stress tensor:

$$b_{ij} = \frac{\langle u'_i u'_j \rangle - \frac{2}{3} K \delta_{ij}}{2K}, \tag{5.1}$$

where $K = \frac{1}{2}\langle u'_i u'_i \rangle$. The three invariants ($I$, II and III) are given by

$$I = b_{ii}, \quad II = -b_{ij}b_{ji}/2, \quad III = b_{ij}b_{jk}b_{ki}/3. \tag{5.2}$$

The various states characterizing the turbulence can be identified by the curve of $-II$ as a function of III (see figure 8*b*). Isotropic turbulence corresponds to $-II = III = 0$. The top of the graph represents the most anisotropic state, called the one-component régime, for which one of the r.m.s. velocity components dominates the other two. The upper branch of the graph represents the two-component régime. The other two boundaries of the graph are representative of axisymmetric states. We compute $-II$ and III in three different constant-z planes at different distances from the lateral wall, corresponding to $z/D_h = 0.5$ (middle plane), $z/D_h = 0.25$ and $z/D_h = 0.05$. The three different planes are identified with different symbols (see figure 8*a*). The arrows

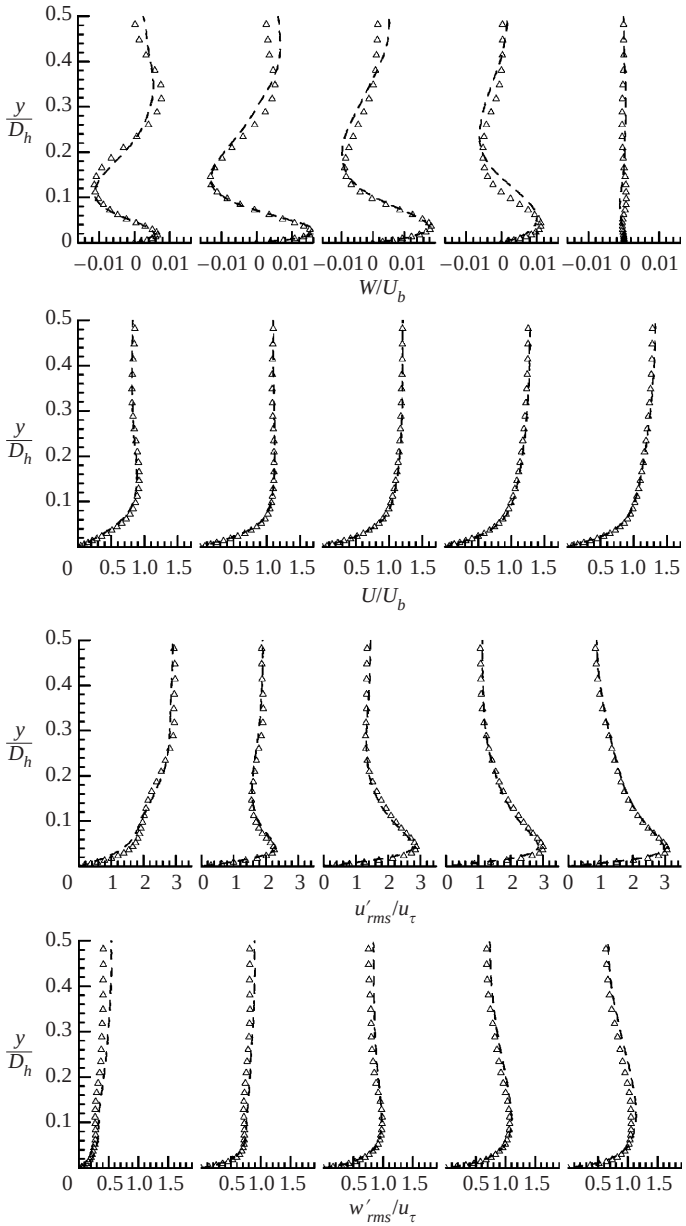

FIGURE 7. For caption see facing page.

on figure 8(*c*) indicate the direction of increasing y (distance from the wall) in each of the three planes: the continuous line corresponds to $z/D_h = 0.5$, the dashed line to $z/D_h = 0.25$ and the dotted line to $z/D_h = 0.05$.

As previously stressed, the turbulence behaviour in the middle plane is similar to a channel flow or a boundary layer. Near the horizontal wall, a classical two-component behaviour is observed due to the strong decrease of the velocity component normal to the wall. A tendency towards a one-component state is observed until $y^+ \approx 9$, where there is a bifurcation along the axisymmetry branch towards a more isotropic state. It is very close to the value found in classical boundary layers where this critical height

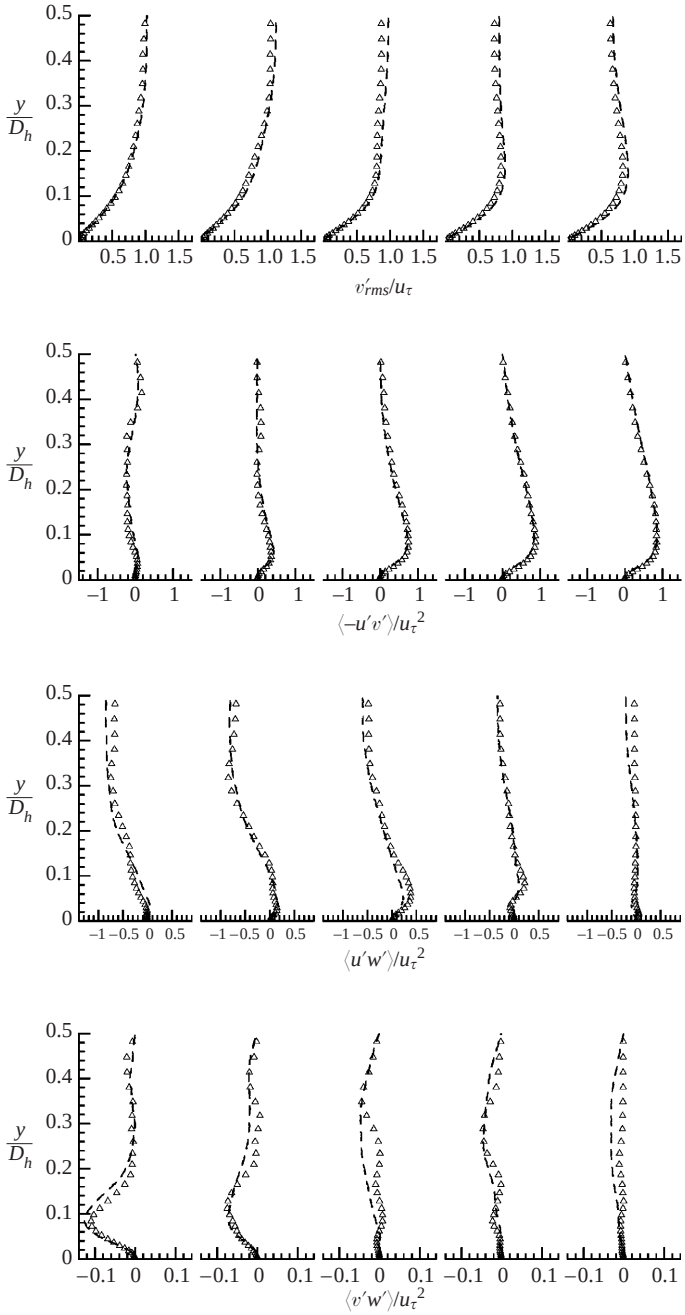

FIGURE 7. Isothermal duct. Comparison between the results of the present LES (△) and DNS of Gavrilakis (1992) (— —) for five z-planes $z/D_h = 0.05$, 0.15, 0.25, 0.35 and 0.5. Values are normalized by the bulk velocity (U_b) for mean streamwise velocity (U) and mean spanwise velocity (W). Values are normalized by the friction velocity ($u_\tau(y,z)$) for r.m.s. of velocities and Reynolds stress.

is located around $y^+ \approx 8$ (see Antonia, Danh & Prabhu 1977). In the duct centre, the turbulence is very close to isotropy. Outside this symmetry plane, the turbulence characteristics are significantly influenced by the lateral wall. For $z/D_h = 0.25$, the turbulence behaviour is analogous to the middle plane in the vicinity of the horizontal

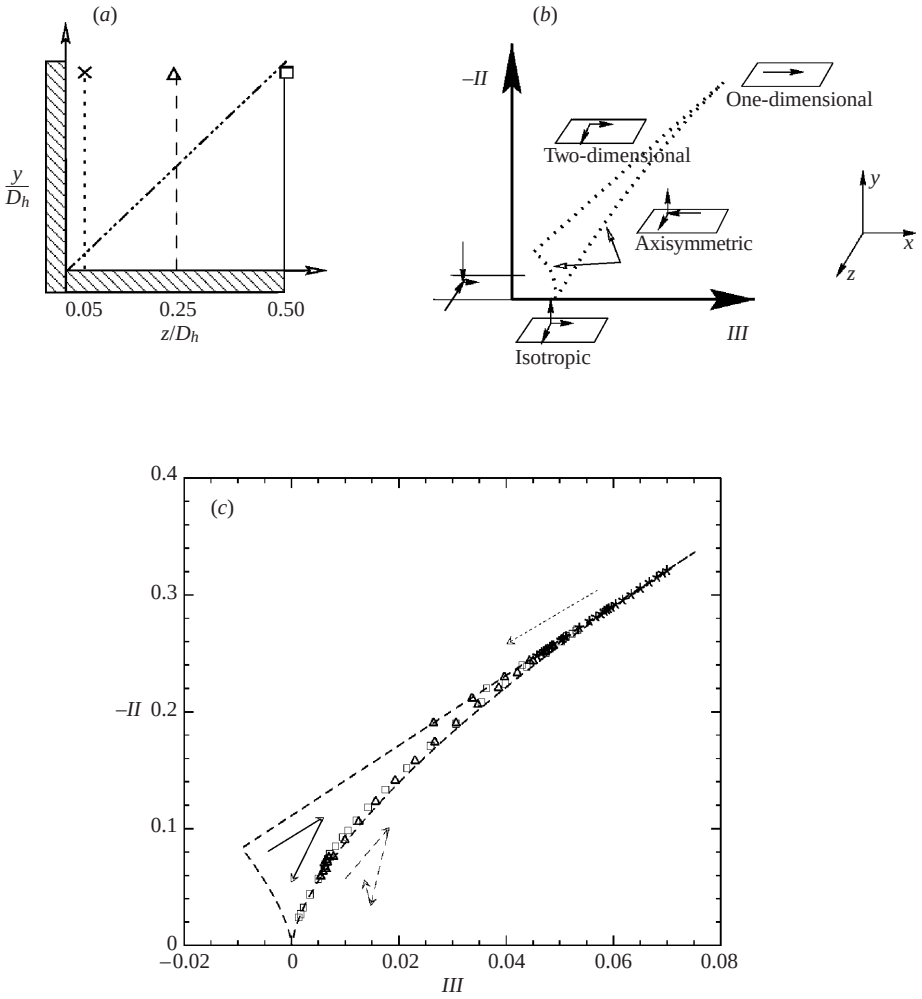

FIGURE 8. Isothermal duct. Anisotropy invariant map for three different z-planes. $z/D_h = 0.05$, 0.25 and 0.5.

wall. However, when the bisector plane of the corner (orientated at 45°) is crossed, the tendency towards an isotropic state is stopped and the axisymmetry branch is followed. The flow behaviour is totally different in the plane closer to the lateral wall. Near the corner, the flow is strongly affected by the presence of both walls and the turbulence corresponds to a one-component régime close to the horizontal wall. When we move away from it, the turbulence moves towards a two-component behaviour. Note that all our computed points are located on Lumley's anisotropy map, which constitutes a quality check for our computation.

6. The heated duct

The geometrical characteristics of the heated ducts are similar to those of the isothermal duct and their physical dimensions are given in § 4.3. The difference with the isothermal duct is the imposition of a higher temperature T_h at the horizontal wall, leaving the other walls at the reference temperature T_w. Three cases of increasing

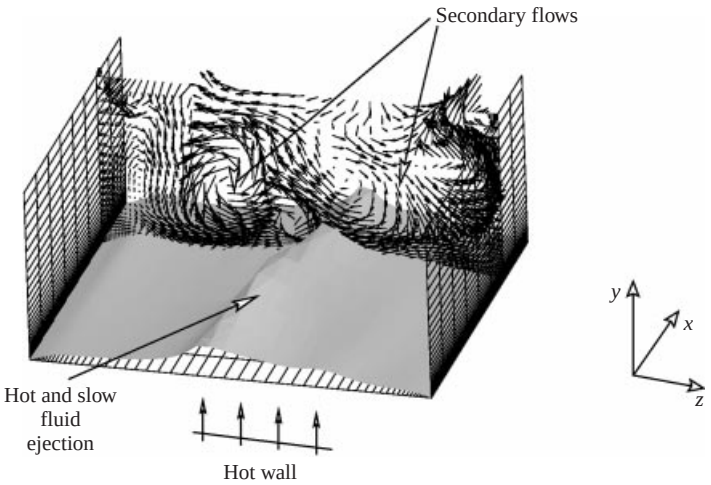

FIGURE 9. Large-scale motion over the hot wall in a heated duct ($T_h/T_w = 2.5$). Instantaneous transversal vector field and an isosurface of temperature corresponding to $T/T_w = 2.1$.

heating intensity are studied corresponding respectively to $T_h/T_w = 1.75$, 2.5 and 3.25. The statistical results are still obtained by averaging in the homogeneous direction (streamwise direction x) and in time. To obtain better statistics, the symmetry with respect to the bisector plane of the hot wall was used by averaging on the two symmetric rectangles formed by this plane.

For turbulent wall flows, the effects of heating on the near-wall turbulence and its structures have been studied experimentally by Wardana, Ueda & Mizomoto (1994, 1995) and Cheng & Ng (1982). It has been shown that strong wall heating induces a significant change in the large-scale motions of the boundary layer. These changes are characterized by the enhancement of the ejections from the heated wall which expel hot and slow fluid from the near-wall region to the fluid interior. This has been visualized both in the experimental work by Cheng & Ng (1982) and in the numerical work by Salinas-Vázquez (1999). In spite of the great amplitude of the instantaneous temperature fluctuations associated with these strong ejections the experimental work did not report a strong influence either on the mean velocity or on the r.m.s. of the velocity fluctuations and the Reynolds stress components statistics. This was confirmed by the plane channel numerical simulation by Salinas-Vázquez (1999). In the channel flow, the random character of the spatial occurrence of the ejections tends to wipe out any significant effects on the various statistical quantities. Conversely, in the heated duct, the enhancement of the size of the ejections above the heated wall and the confinement produced by the lateral wall are such that the hot fluid ejections, for strong enough heating, can only take place in the vicinity of the duct middle plane. The reader is referred to § 7 for a detailed discussion on the generation mechanisms of these turbulent structures. This is clearly displayed on figure 9 which shows the instantaneous secondary flows and the associated ejection region. The constant appearance of the strong ejections near the bisector plane of the heated wall not only creates significant changes in the turbulent intensities but also affects the amplitude of the mean velocity. These effects are clearly illustrated in figure 10(a) which compares the mean secondary flow vectors in one half of the duct section for the heated case ($T_h/T_w = 2.5$) and for the non-heated case. The size and intensity of the mean secondary flows significantly increase when the heating is increased. This is

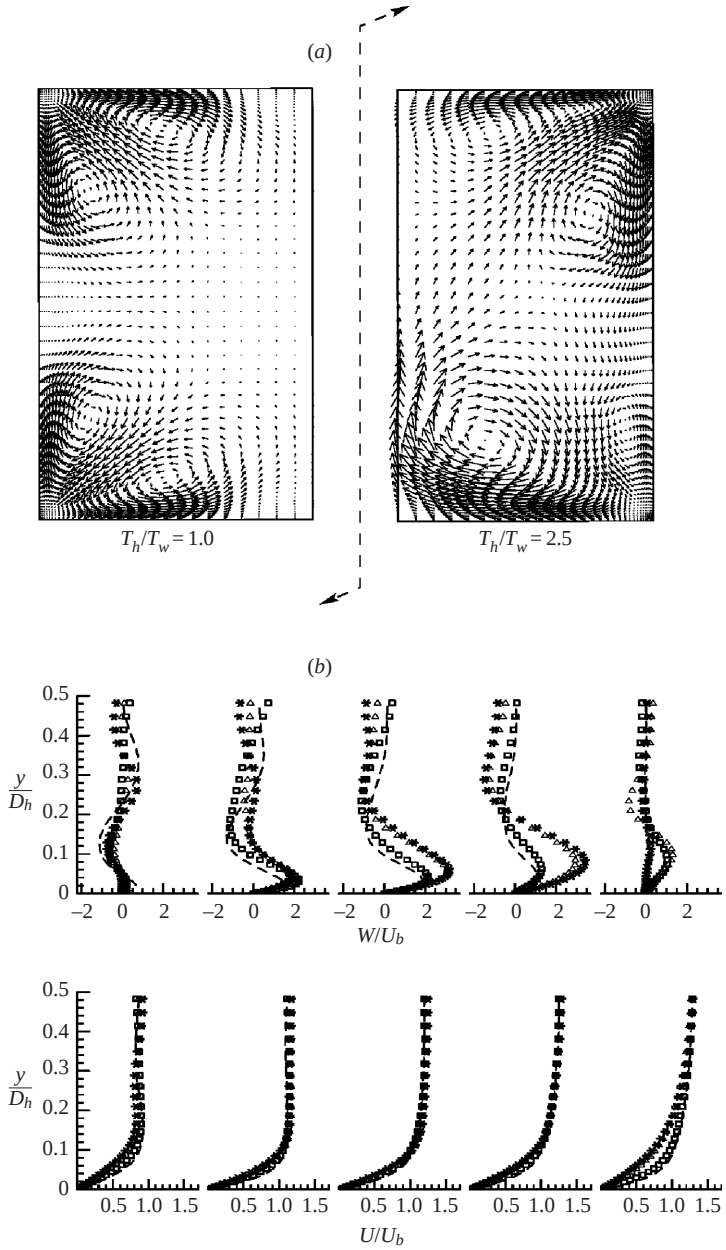

FIGURE 10. (*a*) Cross-section of the mean secondary flow vector field: heated duct ($T_h/T_w = 2.5$) (right) and isothermal duct (left). (*b*) Comparison between the results of the isothermal duct LES (— —) and the heated ducts LES: $T_h/T_w = 1.75$ (□), $T_h/T_w = 2.5$ (△) and $T_h/T_w = 3.25$ (*). Mean streamwise (U) and spanwise (W [×100]) velocities over the hot wall for five z-planes $z/D_h = 0.05$, 0.15, 0.25, 0.35 and 0.5. Values are normalized by the bulk velocity (U_b).

confirmed by the mean velocity profiles displayed in figure 10*b*). Between the middle plane and the corner, the transverse mean velocity exhibits maxima whose amplitude increases with increasing heating intensity. Furthermore, these are located further and further away from the heated wall. This indicates an amplification of both the

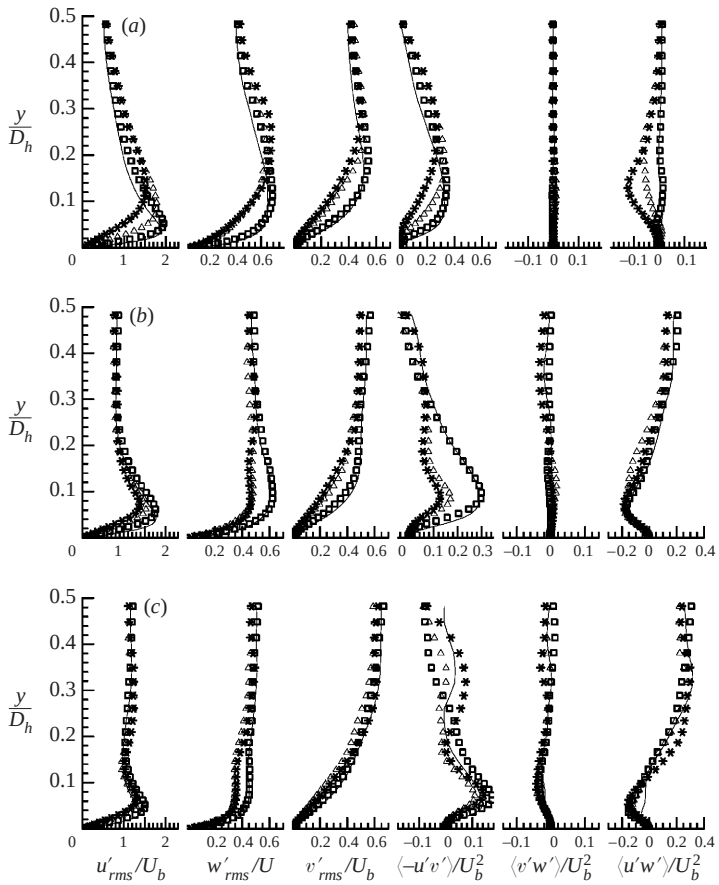

FIGURE 11. Heated ducts. Comparison between the results of the isothermal duct LES (———) and of the heated ducts LES: $T_h/T_w = 1.75$ (□), $T_h/T_w = 2.5$ (△) and $T_h/T_w = 3.25$ (∗) for three z-planes (a) $z/D_h = 0.5$, (b) $z/D_h = 0.25$ and (c) $z/D_h = 0.15$. Values are normalized by the bulk velocity, similar in all cases; r.m.s. are multiplied by 10 and Reynolds stress by 100.

size and the magnitude of these mean secondary flow regions. Compared with the non-heated case, the magnitude of the mean secondary flows is increased by more than 10% for $T_h/T_w = 1.75$ and by more than 50% for $T_h/T_w \geqslant 2.5$. Note that the near-wall shear of the mean streamwise velocity is progressively reduced when the heating increases.

Lets now turn to the second-order statistics related to the fluctuating velocity field. All the quantities shown in figure 11 are normalized with the bulk velocity U_b, which is identical for all the simulated cases. Stronger ejections tend to generate more turbulent activity in the outer part of the boundary layer. However, a competing phenomenon is the enhancement of the viscous dissipation close to the heated wall associated with the viscosity increase with temperature. Indeed in the three planes considered in figure 11, we see a reduction of the three components of the r.m.s. velocity fluctuations in the vicinity of the heated wall. This reduction is particularly obvious in the middle plane of the duct. The peaks of the three components u'_{rms}, v'_{rms} and w'_{rms} are shifted upwards as the heating is enhanced and the turbulent activity is more significant outside the near-wall region. $\langle u'v' \rangle$ is also diminished close to the wall and slightly augmented in the outer region. This is a sign of the reinforcement

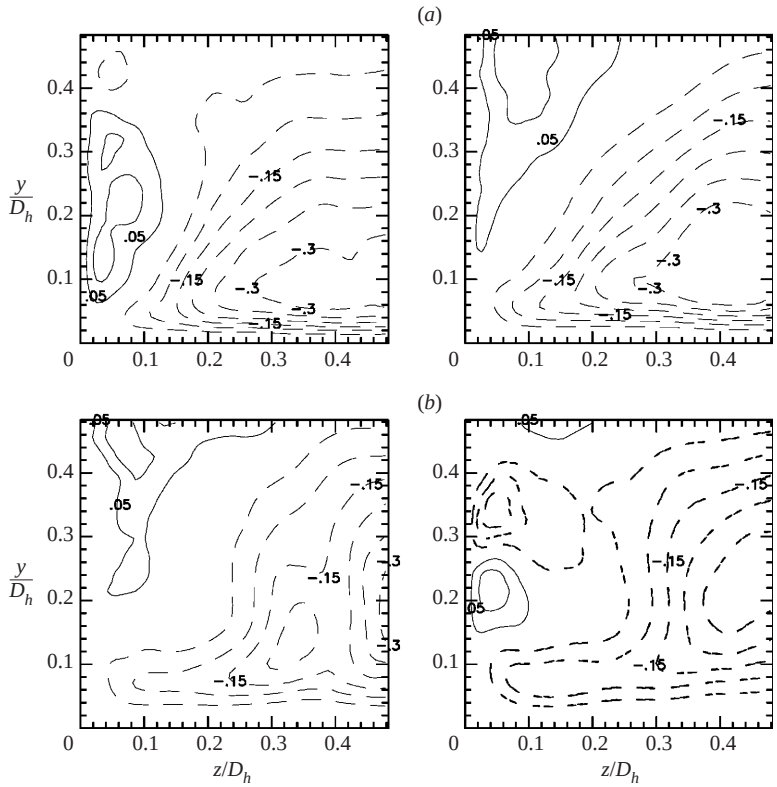

FIGURE 12. Isocontours of the $\langle u'v' \rangle$ Reynolds stress component: (*a*) isothermal (left) and heated duct $T_h/T_w = 1.75$ (right); (*b*) heated duct $T_h/T_w = 2.5$ (left) and heated duct $T_h/T_w = 3.25$ (right). Values are normalized by the bulk velocity.

of the ejections. This trend is not so clear in the corner region where ejections are totally absent. The concentration of turbulent events, ejections and sweeps, in the middle plane is clear on figure 12 which shows the spatial distribution of positive and negative isocontours of $\langle u'v' \rangle$. The negative values corresponding to predominating ejection–sweep mechanisms are more and more concentrated around the middle plane when the heating is enhanced.

The concentration of the ejections in the middle plane region is also clearly noticeable from examination of the variations of the wall shear stress (τ) and the mean wall heat flux q_w along the heated wall (see figure 13). The mean-heat flux is defined as

$$q_w = [\langle \kappa \rangle \, \partial \langle T \rangle / \partial n]_w, \tag{6.1}$$

where κ is defined by (2.7), n designating the direction normal to the wall. Near the duct middle plane, slow and hot fluid is ejected from the wall towards the duct interior. It induces a strong reduction of the wall shear stress in that region in the strongly heated cases. Similarly, the temperature gradient normal to the heated wall is significantly reduced when one compares the weakly and strongly heated cases. Outside the middle plane, the reinforcement of the secondary flows with heating is accompanied by a stronger impingement on the heated wall of the fluid coming from the duct core. It generates more significant velocity gradients and therefore greater

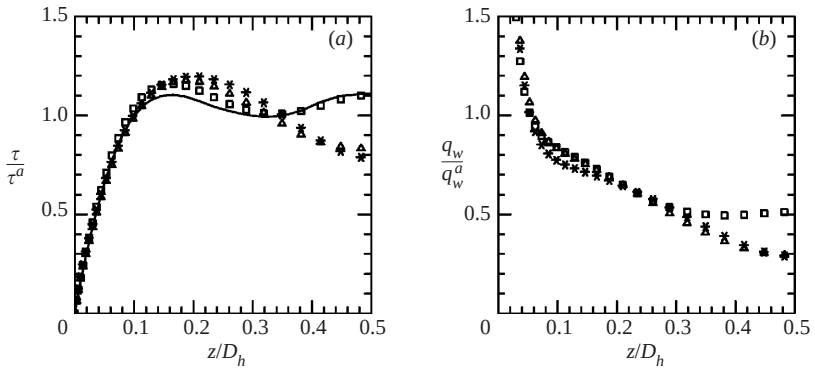

FIGURE 13. Comparison between the results of the isothermal duct LES (— —) and the heated ducts LES: $T_h/T_w = 1.75$ (□), $T_h/T_w = 2.5$ (△) and $T_h/T_w = 3.25$ (∗). (*a*) Local wall shear stress (τ) on the hot wall normalized by the averaged wall shear stress (τ^a) and (*b*) mean wall heat flux (q_w) on the hot wall normalized by the averaged wall heat flux on the hot wall (q_w^a).

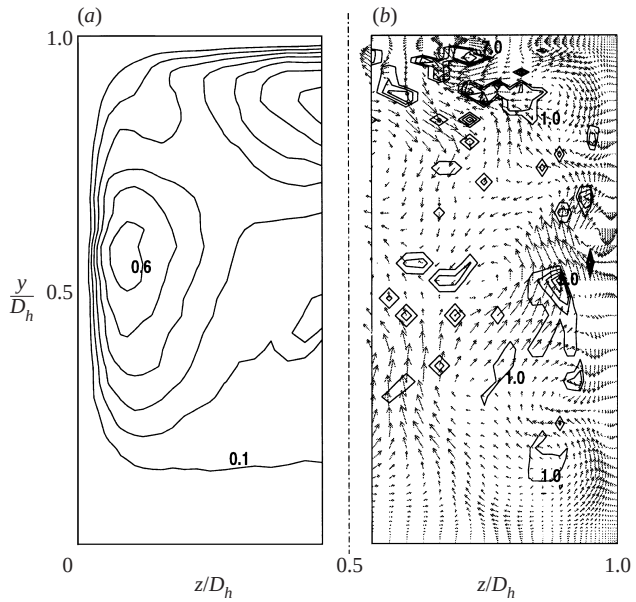

FIGURE 14. Half cross-section of the heated duct at $T_h/T_w = 2.5$: (*a*) contours of the ratio $\langle\mu_t\rangle(y,z)/\langle\mu\rangle(y,z)$ (step 0.1); (*b*) contours of the instantaneous ratio $\mu_t(\boldsymbol{x},t)/\mu(\boldsymbol{x},t)$ (step 1.0), and transversal vector velocity field. The heated wall corresponds to $y/D_h = 0$.

wall shear stress in the region around $z \approx 0.2D_h$. This effect is not so clearly marked for the heat flux.

To end this section, we consider the importance of the subgrid-scale contribution to the statistical quantities such as the Reynolds stresses for instance. Since the fluctuating subgrid-scale part of the field is not explicitly known, this contribution cannot be directly evaluated. The good agreement between our LES and Gavrilakis' DNS shown in § 5 lead us to think that the subgrid-scale contribution is small. More quantitative indications can however be obtained by looking at the importance of the turbulent eddy viscosity relative to its molecular counterpart. Let us consider the dynamic turbulent viscosity $\mu_t(\boldsymbol{x},t) = \rho(\boldsymbol{x},t)v_t(\boldsymbol{x},t)$. Figure 14(*a*) shows a half-cross-

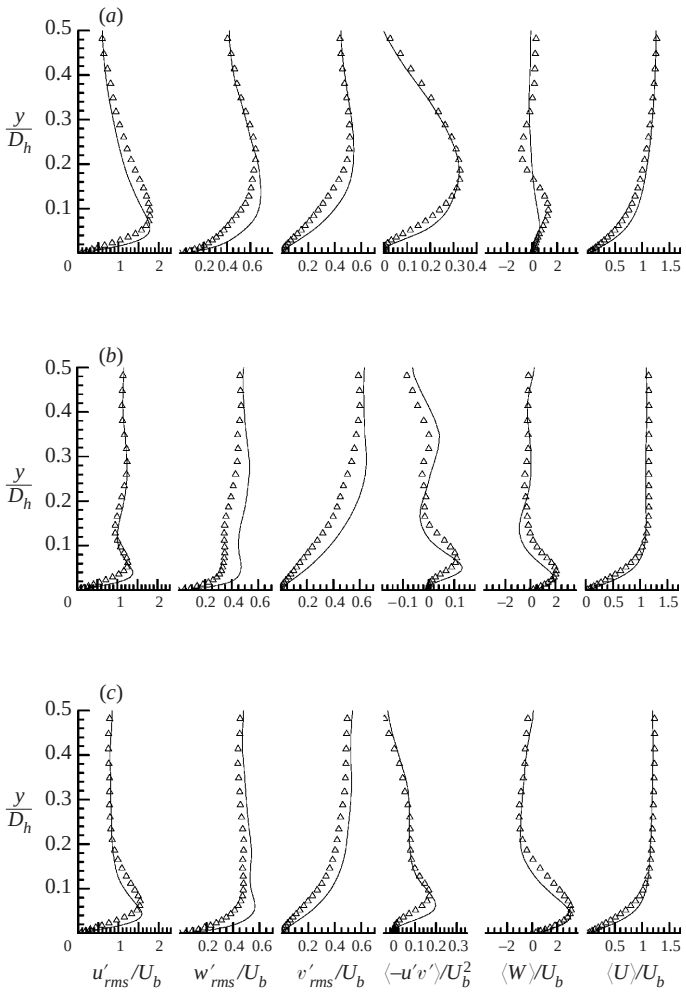

FIGURE 15. Heated duct LES at $T_h/T_w = 2.5$: comparison between the results of the case with a constant molecular viscosity $\mu = \mu(T_w)$ (———) and the case with a molecular viscosity function of temperature (△) (see equation (2.6)) for three planes (*a*) $z/D_h = 0.5$, (*b*) $z/D_h = 0.25$ and (*c*) $z/D_h = 0.15$. Values are normalized by the bulk velocity (U_b), similar in all cases; r.m.s. are multiplied by 10 and Reynolds stress by 100.

section of the ratio of the mean turbulent viscosity over the mean molecular viscosity $\langle\mu_t\rangle(y,z)/\langle\mu\rangle(y,z)$ for the heated duct with $T_h/T_w = 2.5$. The maximum values remain small and are of the order of 0.7. As expected, these are concentrated in the regions of highest turbulent activity (see figure 12), that is to say close to the cold and the lateral wall more particularly around their bisector plane. Furthermore, the mean turbulent viscosity remains very weak over the hot wall. It is important to notice that, although the ratio of the mean quantities is small, the instantaneous turbulent viscosity can be locally as large as ten times its molecular counterpart. Figure 14(*b*) shows, at a particular instant, a half-cross-section of the instantaneous ratio $\mu_t(\boldsymbol{x},t)/\mu(\boldsymbol{x},t)$ for the heated duct with $T_h/T_w = 2.5$. The projection of the instantaneous velocity field on the cross-section is also represented. At this particular instant, the ratio reaches values up to about 10 in very localized regions of the flow. This clearly demonstrates

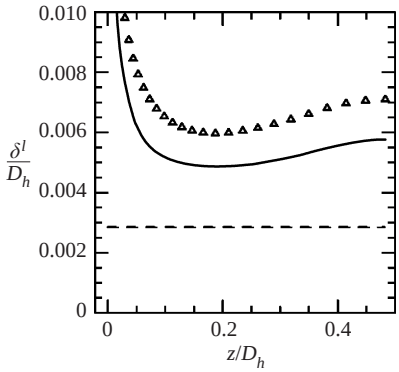

FIGURE 16. Viscous thickness δ^l in the heated duct LES at $T_h/T_w = 2.5$: comparison of the case with a constant molecular viscosity $\mu = \mu(T_w)$ (———) and the case with a molecular viscosity function of temperature (△) (see equation (2.6)). The dashed line (— —) represents the averaged viscous thickness δ^a for the isothermal duct.

the crucial rôle played by the turbulent viscosity in these particular flow regions and the necessity to efficiently model the action of the subgrid scales.

6.1. *Viscosity effects*

To clearly identify the effects associated with the variations of the viscosity with temperature, we have compared our previous $T_h/T_w = 2.5$ heated-duct LES with variable viscosity to another LES which is identical except for the viscosity which is now kept constant with a value $\mu = \mu(T_w)$. The comparison of the statistics is shown in figure 15. The change in viscosity significantly affects both the mean velocity profiles and the statistics based upon the fluctuating field and these effects are felt from the middle plane to the duct corner. Furthermore, figure 15 reveals that the increase of the viscosity close to the wall, compared to the constant viscosity case, has similar effects on the statistics to an enhancement of the wall heating. Indeed, as far as the mean flow is concerned, the secondary transverse flow is enhanced in the variable viscosity case and the longitudinal velocity shear is less pronounced at the wall. Figure 16 compares, for the variable and constant viscosity cases, the variations of the viscous length at the heated wall with the distance from the lateral wall. The increase in viscosity is accompanied by an increase of the viscous length over the whole heated wall. It is established that the size of the low-speed and high-speed streaks scales with the viscous thickness and an increase of the latter will automatically induce an enlargement of the streaky structures. This is confirmed by the u'_{rms} profile shown on figure 15 which displays a peak situated further away from the heated wall in the variable viscosity case. It is now commonly accepted that the ejection mechanism is intimately linked with the near-wall low-speed streaks: an augmentation of the streak size in the middle plane is therefore accompanied by an enhancement of the size of the hot fluid ejections. This triggers larger secondary transverse flows as reflected in the statistics. The increase of the size of the turbulent structures in the vicinity of the heated wall is investigated in greater detail in § 7.

The effects of the heating on the statistics near the horizontal wall opposite to the heated wall are investigated. Despite the significant changes observed on the hot wall, figure 17 shows that the statistics are not strongly modified near the cold wall compared to the non-heated case. Near the wall bisector, one may however notice an increase in the statistical quantities related to the fluctuating normal component v'

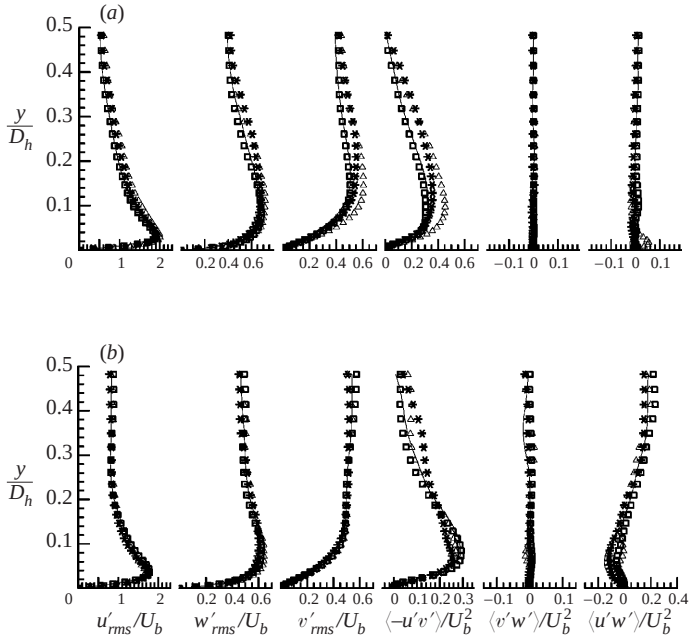

FIGURE 17. Comparison between the results of the isothermal duct LES (— —) and the heated ducts LES: $T_h/T_w = 1.75$ (□), $T_h/T_w = 2.5$ (△) and $T_h/T_w = 3.25$ (*) for the cold wall opposite to the hot one at (*a*) $z/D_h = 0.5$ and (*b*) $z/D_h = 0.25$. Values are normalized by the bulk velocity (U_b); r.m.s. are multiplied by 10 and Reynolds stress by 100.

both for its r.m.s. profile and for the profile of the Reynolds stress component $\langle u'v' \rangle$. This is a another signature of the enhancement of the ejections taking place at the heated wall and which affect the v' field in the whole duct.

7. Turbulent structures

In the previous section, we have mentioned the increase in size of the ejections due to the increase in size of the streaky structures. We will now proceed to reinforce this argument by examing the flow structures.

7.1. *Low- and high-speed streaks*

First, we will consider the streaks. Figure 18(*a*) shows the contours of the longitudinal velocity fluctuations near the hot wall and one of the walls of the isothermal duct. The classical streaky structures of the turbulent boundary layer are clearly visible and their width is significantly enhanced near the heated wall. This streak enlargement can be more quantitatively estimated by examination of the transverse correlation of the longitudinal velocity correlation (see figure 18*b*). The negative peak indicates half of the transverse wavelength of the low- and high-speed streaks. Let us denote by λ this transverse wavelength. When normalized by the hydraulic diameter D_h, it is clear that the streak spacing increases when the heating is augmented. Figure 18(*b*) and table 2 indeed indicate that the streak spacing $\lambda/2$ saturates for a value close to $\approx 0.3D_h$ with no significant variations between the case $T_h/T_w = 2.5$ and the case $T_h/T_w = 3.25$. This saturation can be understood with the following argument: if streaky structures are present, it is reasonable to think that their minimal number has to be three. Indeed, one low-speed current is associated with ejections of fluid from the

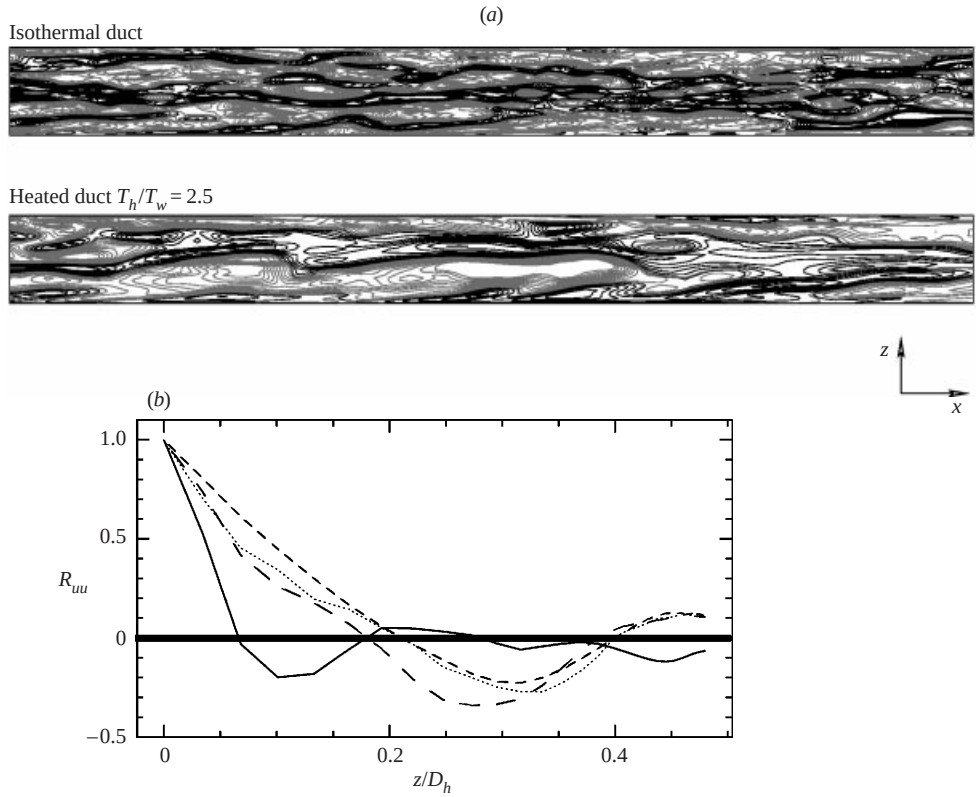

FIGURE 18. (*a*) Fluctuating streamwise velocity contours near a wall of the isothermal duct ($y^+ = 13$) and near the heated wall ($y^+ = 16$) of the heated duct ($T_h/T_w = 2.5$). The contours are between $-0.3 < u'(\boldsymbol{x},t)/U_b < 0.3$ ($u'(\boldsymbol{x},t) = u(\boldsymbol{x},t) - \langle u\rangle(y,z)$, see §4.2). Positive contours are light ($(u'(\boldsymbol{x},t)/U_b) > 0$) and negative contours dark ($(u'(\boldsymbol{x},t)/U_b) < 0$). (*b*) Spanwise two-point correlation of the streamwise velocity for the heated ducts $T_h/T_w = 3.25$ ·····, $y^+ = 19$, $T_h/T_w = 2.5$ – – –, $y^+ = 16$, $T_h/T_w = 1.75$ — —, $y^+ = 14$ and isothermal duct ———, $y^+ = 13$.

wall. This ejected fluid has to be compensated by sweeping motions and high-speed streaks on both sides of the low-speed streak. One can therefore conclude that the maximum spanwise size of the streaky structures will be approximately one third of the duct width. In this configuration, the low-speed streak will be located around the central plane of the duct and surrounded with high-speed streaks associated with the engulfment of fluid from the duct core towards the heated wall. In §6.1, we argued that the increase in size of the flow structures near the heated wall can be mainly attributed to the viscosity augmentation. We then compute the transverse wavelength λ^+ normalized by the viscous thickness δ^a defined in §4.2 (see table 2). We notice a slight augmentation of λ^+ in the two heated cases satisfying $T_h/T_w \leqslant 2.5$ compared to the non-heated case. λ^+ however remains close to the traditional value of 100 found in classical turbulent boundary layers and channel flows. For the most strongly heated case $T_h/T_w = 3.25$, the saturation due to the duct size implies a lower value of λ^+.

7.2. *Quasi-longitudinal vorticity structures*

In figure 19, we compare the flow structures present in the vicinity of the hot wall corresponding to the $T_h/T_w = 2.5$ case with the structures of the isothermal duct.

T_h/T_w	δ^a/D_h	λ/D_h	λ/δ^a
1.0	0.0024	0.202	≈ 85
1.75	0.0049	0.540	≈ 110
2.5	0.0068	0.634	≈ 93
3.25	0.0090	0.672	≈ 75

TABLE 2. Streak size.

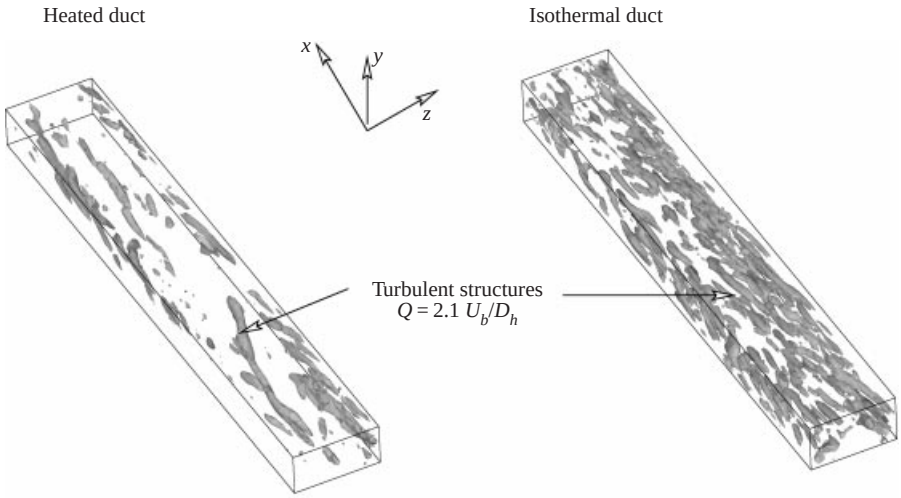

FIGURE 19. Visualization of turbulent structures in the heated duct ($T_h/T_w = 2.5$) and in the isothermal duct through the Q criterion (Hunt *et al.* 1988), $Q = 1.6U_b/D_h$.

Flow structures are identified here using the so-called Q criterion (Hunt, Wray & Moin 1988) which is based upon the second invariant of the velocity gradient tensor, $Q = \frac{1}{2}(\Omega_{ij}\Omega_{ij} - S_{ij}S_{ij})$, where $\boldsymbol{\Omega}$ is the antisymmetrical part and $\boldsymbol{S}$ the symmetrical part. The positive-Q regions have proven to be a good indicator of the coherent vortices in various wall-bounded or free-shear flows (see e.g. Dubief & Delcayre 2000). The three-dimensional visualizations of figure 19 show the presence of longitudinally elongated structures in both isothermal and heated cases. The size of these structures both in diameter and length is however noticeably enhanced in the heated case and they are more concentrated around the wall bisector.

The understanding of the link between longitudinal vortices and low- and high-speed streaks constitutes an old debate of the chicken-and-egg type, with the goal being to try to determine which generates the other. This is still an open issue that we shall not address here, our main objective being to investigate the effect of wall heating on the various flow structures. Figure 20 (bottom) shows that there exists a close relationship between the longitudinal vortices and the low- and high-speed streaks, since these vortices are always situated in the interfacial region between the streaks (see Robinson 1991). As shown in figure 9 the low-speed streak which corresponds to slow and hot fluid coming from the wall is clearly identified by the folding of the temperature isosurface close to the heated wall. This folding exhibits longitudinal oscillations of large wavelength. It is bordered by a succession of longitudinal structures identified by the Q criterion which are associated with violent ejections of hot fluid from the wall towards the duct core.

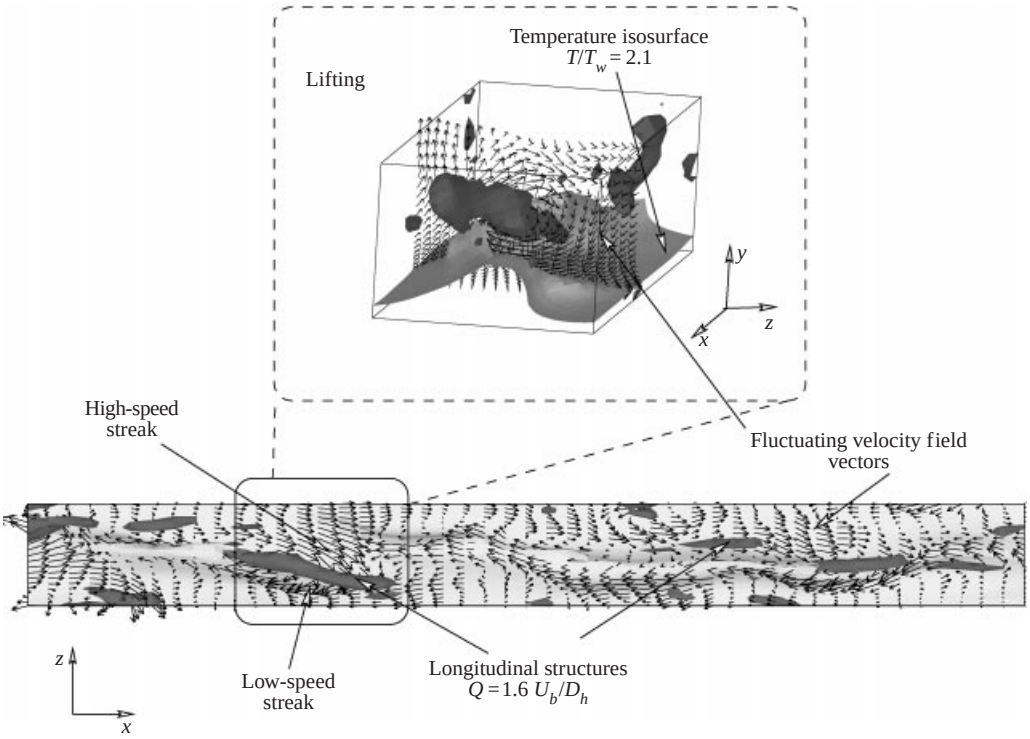

FIGURE 20. Visualization of an ejection and of the lifting mechanism.

7.3. *Ejections*

In figure 20 (top), we have isolated a strong ejection event which is linked with a longitudinal turbulent structure. They are similar in nature to those observed in the isothermal case but of much greater size and intensity. The rôle played by compressibility effects is investigated at the end of this section. To get a more complete picture of the longitudinal structures, the vortex lines associated with these events are plotted in figure 21. It shows that the observed longitudinal structures do not correspond to vortex line concentrations but the Q isosurfaces are in fact the signature of the quasi-longitudinal legs of several hairpin vortices organized in succession, orientated in the longitudinal direction.

A classical way of identifying ejections and sweeps is to perform a quadrant analysis of the Reynolds stress component $\langle u'v' \rangle$. This involves the decomposition of this component as a function of the sign of the two fluctuating velocity components that compose it. There are therefore four quadrants $\langle (+u')(+v') \rangle_1$, $\langle (-u')(+v') \rangle_2$, $\langle (-u')(-v') \rangle_3$ and $\langle (+u')(-v') \rangle_4$, where the plus sign and the minus sign correspond to positive or negative values of the fluctuations. Willmarth & Lu (1972) showed, in a boundary layer, that quadrants two and four are respectively related to the turbulent ejections and to the turbulent sweeping motions. Figure 22 shows the profile of $\langle (-u')(+v') \rangle_2$ and $\langle (+u')(-v') \rangle_4$ in the duct middle plane $z/D_h = 0.5$ and in the plane $z/D_h = 0.25$ both for the isothermal duct and the heated duct ($T_h/T_w = 2.5$). In the wall bisector, the regions of maximum activity of both the ejections and the sweeping motions, which correspond to the minima of $\langle (-u')(+v') \rangle_2$ and $\langle (+u')(-v') \rangle_4$ curves, are shifted further away from the wall in the heated case. This seems to

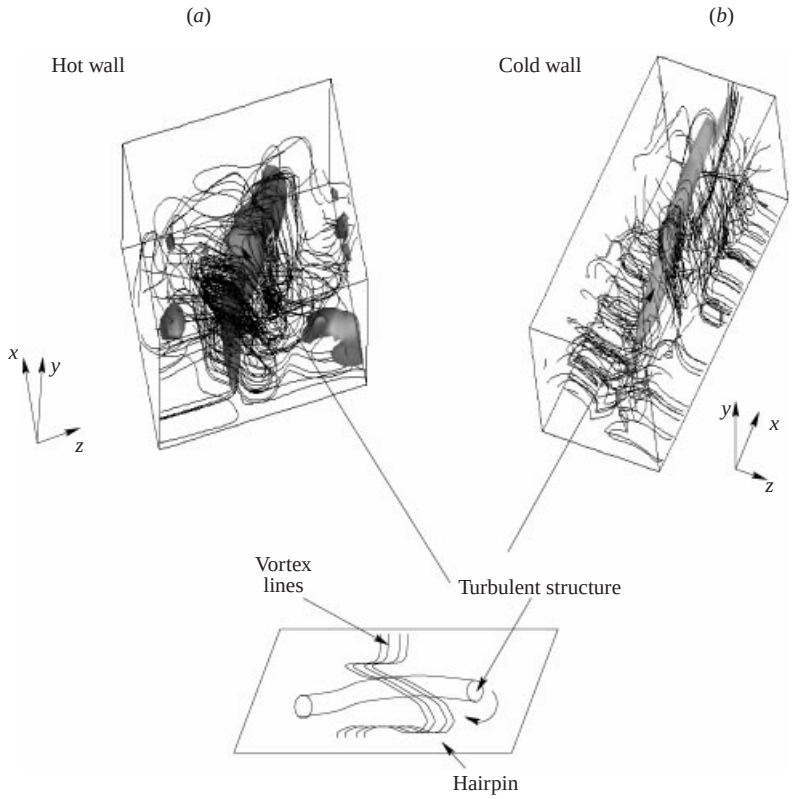

FIGURE 21. Turbulent structure, $Q = 2.1U_b/D_h$ isosurface, and vortex lines. (a) Heated duct at $T_h/T_w = 2.5$ and (b) isothermal duct.

indicate an enhancement of the size of these motions in global units. However, for the heated case and the duct bisector plane, the normalized $\langle(-u')(+v')\rangle_2$ profile exhibits a plateau of near constant value around -0.0018 for $0.2 \lesssim y/D_h \lesssim 0.3$ with a minimum located around $y/D_h = 0.26$ which indicates the location of maximum intensity of the ejections. With the help of table 2, one can easily check that this minimum corresponds in wall units to $y = 38\delta^a$ where δ^a is defined in § 4.2. In the non-heated case, the middle-plane minimum value for $\langle(-u')(+v')\rangle_2$ is reached around $y/D_h = 0.10$, that is to say for $y = 42\delta^a$ (see table 2). This signifies that the size of the ejection in wall units is nearly identical in the non-heated and the heated cases. Figure 22 confirms that the ejections and sweeping motions are mainly concentrated near the duct middle plane. Indeed, the quadrant analysis at $z/D_h = 0.25$ indicates a significant reduction of both $\langle(-u')(+v')\rangle_2$ and $\langle(+u')(-v')\rangle_4$ components compared with the duct bisector and with the isothermal case. This result confirms the previous flow visualizations where turbulent structures were more concentrated near the duct middle plane in association with the central low-speed streak.

The vorticity associated with the streaky structures, the ejections and the sweeps can be quantified through the profiles of the fluctuating vorticity components. Let $\boldsymbol{\omega} = \nabla \times \boldsymbol{u}$ be the vorticity vector and $\boldsymbol{\omega}' = (\omega_x', \omega_y', \omega_z')$ the fluctuating vorticity vector. Figure 23 represents the y-profile of $\omega'_{x\,rms}$, $\omega'_{y\,rms}$ and $\omega'_{z\,rms}$ normalized by U_b/D_h in both planes $z/D_h = 0.5$ and $z/D_h = 0.25$. The distance y from the wall is normalized by δ defined by (4.7). In the non-heated duct (figure 23b), the qualitative

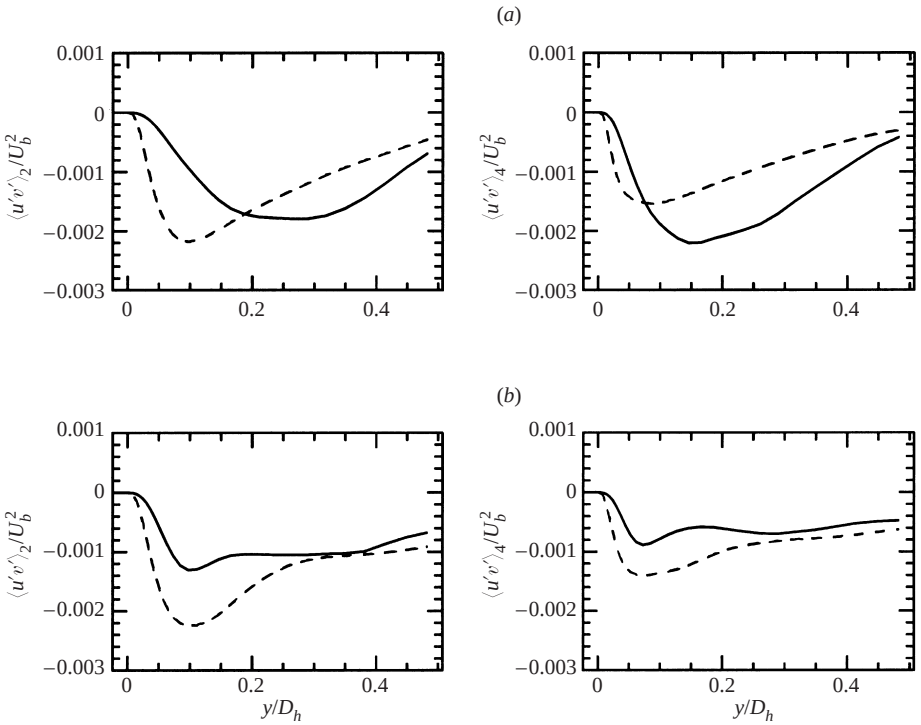

FIGURE 22. Quadrant analysis of the Reynolds shear stress component ($\langle u'v'\rangle$) for the isothermal duct (— —) and heated duct $T_h/T_w = 2.5$ (———). We compare the ejections (second quadrant $\langle u'v'\rangle_2$, (left)) and the sweeping motions (fourth quadrant $\langle u'v'\rangle_4$, (right)) for two z-planes: (*a*) $z/D_h = 0.5$ and (*b*) $z/D_h = 0.25$. Values are normalized by the bulk velocity (U_b).

behaviour of the vorticity components is similar to the classical turbulent channel flow (see Lamballais, Lesieur & Métais 1997). The maximum vorticity produced is spanwise and at the wall. This constitutes a signature of the high-speed streaks where the sweeps produce high values of the local spanwise vorticity at the wall. The r.m.s. vorticity perpendicular to the wall is higher than the longitudinal vorticity in the region $5 \lesssim y^+ \lesssim 50$. This is another statistical indicator of the streaks. The vorticity distribution is nearly isotropic near the duct centre with a nearly equal repartition between the three r.m.s. components. Compared to the middle plane, the spanwise vorticity component is significantly reduced at the wall in the $z/D_h = 0.25$ plane, indicating a weakening of the sweeping motions. Both the location and the amplitude of $\omega'_{y\,rms}$ are however identical in both planes. When heating is applied with $T_h/T_w = 2.5$, the spanwise component no longer dominates the other two components, except in the near-wall region of the middle plane (figure 23*a* (right)). In this region, the strong rise observed in the non-heated case is significantly reduced. This reduction is attributable to the enhanced viscous effects when heating is applied and also to the fact that the central region of the duct is most of the time occupied by the low-speed streak. The maximum of $\omega'_{z\,rms}$ is shifted slightly further away from the wall compared to the non-heated case. An interesting feature is the local maximum of $\omega'_{x\,rms}$ around $y^+ \approx 30$. In global units, this location corresponds to $y \approx 0.2D_h$ which is the beginning of the plateau of negative values for $\langle(-u')(+v')\rangle_2$ observed in figure 22 and which corresponds to a region of the strongest ejection activity. This demonstrates that longitudinal vorticity generation is strongly linked with the ejection

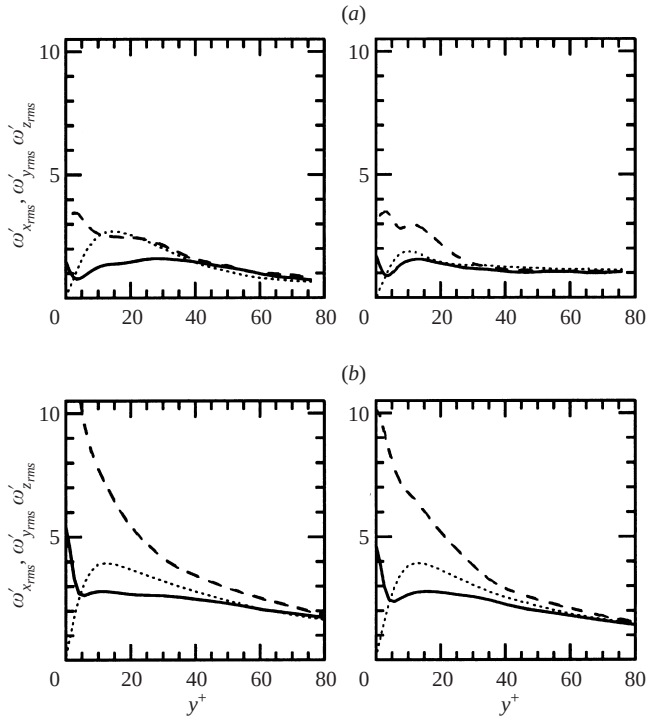

FIGURE 23. Vorticity r.m.s. profiles ($\omega'_{x\,rms}$ (———), $\omega'_{y\,rms}$ (– – –) and $\omega'_{z\,rms}$ (— —)) for (b) the isothermal duct and (a) the heated duct $T_h/T_w = 2.5$, for two z-planes: $z/D_h = 0.5$ (left) and $z/D_h = 0.25$ (right). Vorticity values are normalized by the bulk velocity (U_b) and hydraulic diameter (D_h) and the distance from the wall by the viscous thickness δ.

process as shown with the vortex lines plotted in figure 21. In the $z/D_h = 0.25$ plane, the local maximum of the longitudinal fluctuating vorticity is shifted much closer to the wall in correspondence with the $\langle(-u')(+v')\rangle_2$ profile of figure 22. The reduced streaky activity in this plane can be seen through the reduction of the peak of $\omega'_{z\,rms}$. It is important to note that the vorticity level is significantly reduced in the heated case in comparison with the non-heated case when the vorticity is normalized with the global unit U_b/D_h. However, the vorticity could also be normalized by the wall unit u^a_τ/δ^a where u^a_τ is the average of u_τ (defined by (4.5)) over the four duct walls in the non-heated case and over the heated wall in the case with heating. δ^a is defined in §4.2. We found $u^a_\tau/\delta^a \approx 27.3U_b/D_h$ in the non-heated case and $u^a_\tau/\delta^a \approx 3.6U_b/D_h$ in the heated case. With a choice of u^a_τ/δ^a as a unit for the vorticity the values shown in figure 23 have then to be divided by 27.3 in the non-heated case and by 3.6 in the heated case. This second scaling is certainly more representative of the vorticity generation associated with the ejection mechanism, since the ejections induce a lift-up and a stretching of the vortex lines, which are originally situated in the near-wall region.

Figure 24 compares, in the middle plane, the longitudinal vorticity in the non-heated and in the heated cases using the wall-unit non-dimensionalization. It is clear that the longitudinal vorticity generation is significantly enhanced when heating is applied in relation to the stronger ejections.

A clearer view of the ejection process can be acquired by selectively considering the (y, z)-planes where violent ejections take place. We select these planes in the

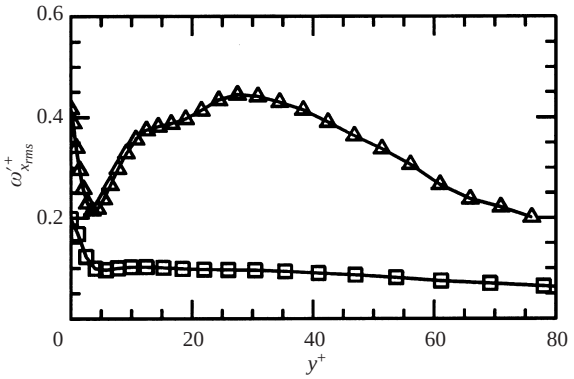

FIGURE 24. Comparison of the streamwise vorticity r.m.s. ($\omega'_{x\,rms}$): isothermal duct (□) and heated duct $T_h/T_w = 2.5$ (△). Vorticity values are normalized by the friction velocity ($u_\tau(y,z)$) and the viscous thickness δ.

following way: in each transverse plane we consider the point on the wall bisector ($z_E = 0.5D_h$) situated at a distance y_E from the heated wall and corresponding to the minimum of the second quadrant $\langle u'v'\rangle_2$. The case we consider below is the heated case $T_h/T_w = 2.5$; we checked from figure 22 that $y_E \approx 0.26D_h$. We then apply the following conditional sampling:

$$D(Ejec) = \begin{cases} 1 & \text{if } u'(y_E, z_E) < 0,\ \ v'(y_E, z_E) > 0 \text{ and} \\ & \quad (u'v'(y_E, z_E)/\langle u'v'\rangle(y_E, z_E)) \geqslant 10 \\ 0 & \text{otherwise.} \end{cases} \tag{7.1}$$

If $D(Ejec) = 1$ we take into account the associated transversal plane in the statistical sampling; if $D(Ejec) = 0$ the corresponding plane is discarded. The statistics are then obtained with all the transversal planes that fulfil the previous condition with a statistical sampling of several hundred instantaneous records. The statistics are then representative of several similar ejection events and do not focus on one isolated event only. Figure 25(a) displays the averaged transverse velocity field resulting from this statistical sampling. Only the bottom half of the duct near the heated wall is shown. Note that the averaging process masks any asymmetry, producing a symmetrical averaged structure. The ejection process and the two associated longitudinal vortices are clearly identified. In figure 25, the mean transverse field and the conditionally averaged tranverse fields are compared for one quarter of the duct (part b and c respectively). It clearly shows that the cores of the longitudinal vortices associated with the ejection process are situated closer to the duct middle plane and further away from the heated wall than the mean-field longitudinal vortices. Their core is situated at a distance of $\approx 0.25D_h$ from the heated wall ($y \approx 37\delta^a$).

Until now, we have mainly concentrated on the enhancement of the size of the various flow structures, but we have not yet investigated the possible effects of density differences on the ejections, such as flow expansion or compression effects. We still consider the conditionally averaged field shown on figure 25. Figure 26 shows the contours of the two conditionally averaged velocity derivatives $\partial w/\partial z$ and $\partial v/\partial y$ in the cross-sections associated with the ejections. Figure 26 also displays the divergence of the velocity projected on the cross-section $(\boldsymbol{\nabla}\cdot\boldsymbol{u})_p = \partial v/\partial y + \partial w/\partial z$ which is representative of the total velocity divergence since the remaining contribution corresponding to $\partial u/\partial x$ turns out to be small in comparison with the other derivatives. Note that compressibility effects associated with local expansion or compression are

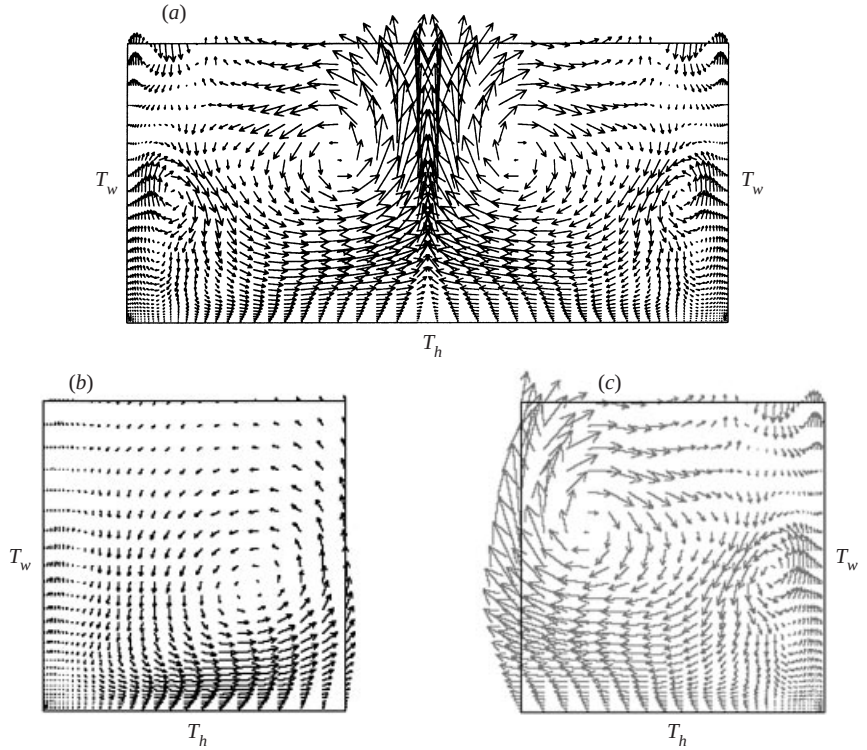

FIGURE 25. Heated duct LES at $T_h/T_w = 2.5$: (*a*) and (*c*) mean conditioned transversal vector field (one half and one quarter of the duct cross-section respectively); (*b*) mean transversal vector field (one quarter of the duct cross-section).

important since the maximum and the minimum of $(\nabla \cdot \boldsymbol{u})_p$ in the selected planes are approximately $1.19U_b/D_h$ and $-1.05U_b/D_h$. As already noticed on figures 22 and 23, the maximum of ejection activity, in the middle plane, is situated around $y/D_h \approx 0.3$. This flow region clearly separates two flow regimes: a region of flow convergence with positive $(\nabla \cdot \boldsymbol{u})_p$ for $y \lesssim 0.28D_h$ and a region of flow divergence with negative $(\nabla \cdot \boldsymbol{u})_p$ for $y \gtrsim 0.28D_h$. As shown in figure 20, at the foot of the ejection, the rise of the hot fluid from the heated wall induces an entrainment of the colder fluid from the duct core towards the hot wall. This engulfment mechanism can be observed both with the conditionally averaged temperature field shown in figure 26 and with the instantaneous visualization of the temperature fluctuations associated with a single ejection event displayed in figure 27. This last figure clearly shows that cold fluid, corresponding to $T'(\boldsymbol{x}, t) < 0$ ($T'(\boldsymbol{x}, t) = T(\boldsymbol{x}, t) - \langle T \rangle(y, z)$), accumulates at the bottom of the ejection where it expands and generates a strong flow divergence. This constitutes an amplification mechanism for the ejection process. This expansion is mainly directed towards the vertical direction with the main contribution coming from positive $\partial v/\partial y$ (see figure 26). The lateral expansion is indeed limited by the laterally converging fluid associated with the secondary flow and marked by the negative value of $\partial w/\partial z$ on the border of the expanding region. Conversely, at the top of the ejection, the hot fluid extracted from the wall reaches colder flow regions and then tends to undergo a significant compression. This compression is bordered by laterally diverging fluid indicated by the regions of positive $\partial w/\partial z$ (see figure 26). Finally, we investigated the effects associated with vorticity generation

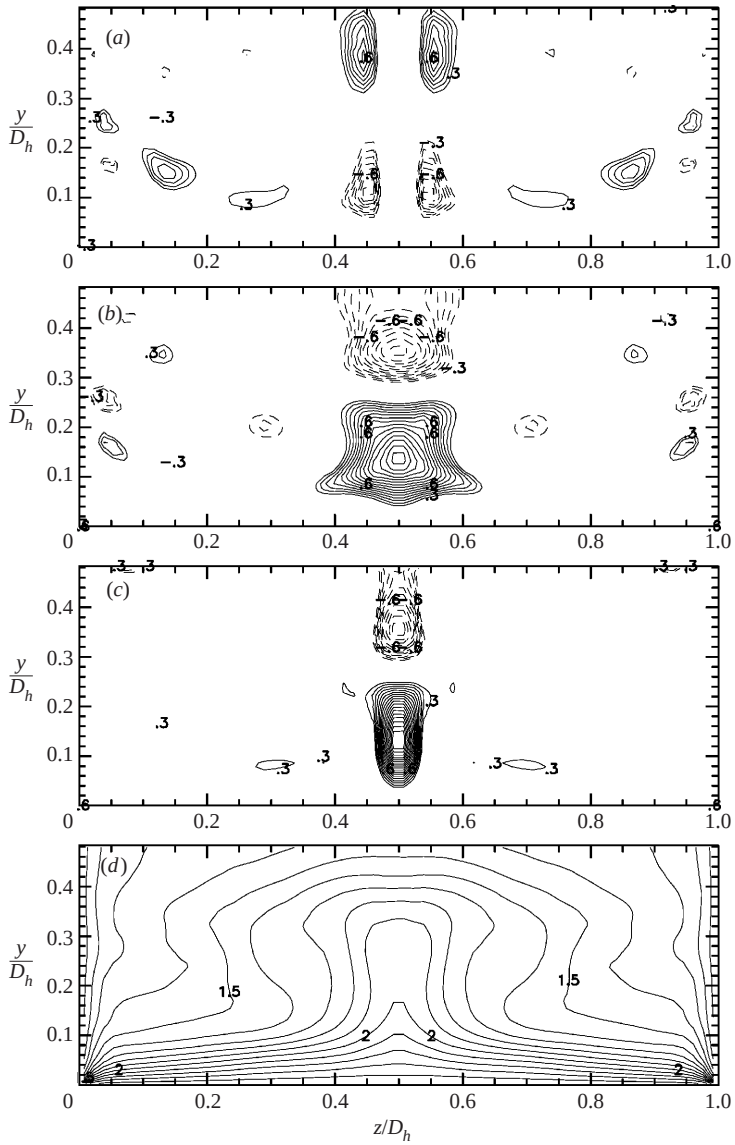

FIGURE 26. Conditionally averaged statistics. (*a*) $\partial w/\partial z$, step $0.05(U_b/D_h)$; (*b*) $\partial v/\partial y$, step $0.05(U_b/D_h)$; (*c*) divergence of the velocity projected on the cross-section $(\nabla \cdot \boldsymbol{u})_p$, step $0.05(U_b/D_h)$; and (*d*) mean temperature, step $0.1T_w$. Positive values (———) and negative values (— —).

associated with baroclinic effects: we were unable to clearly identify regions of the ejections dominated by these effects.

8. Conclusion

We have performed large-eddy simulations (LES) of the three-dimensional compressible Navier–Stokes equations to study the turbulent flow within a duct of square cross-section. We have successively considered a non-heated duct for which a given temperature is prescribed at the four walls and a heated duct for which a higher temperature is imposed at one of the walls. The low Mach number of our

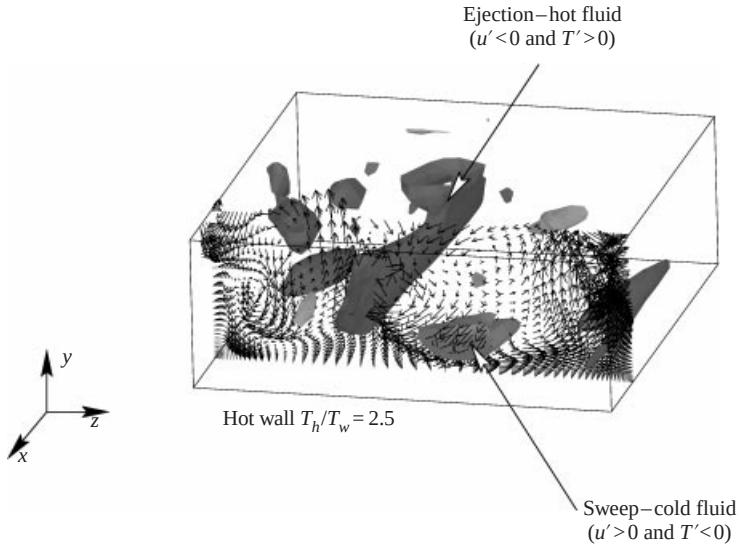

FIGURE 27. Fluctuating velocity vector field and fluctuating temperature isosurfaces $T'(\boldsymbol{x}, t) = 0.3T_w$ (dark) and $T'(\boldsymbol{x}, t) = -0.3T_w$ (light).

computations has allowed a precise comparison with the previous DNS and LES incompressible results. We have centred our comparisons on Gavrilakis' (1992) DNS. A very good concordance with the DNS results was achieved by the LES. The LES turn out to be able to correctly reproduce both the statistical quantities and the turbulent structures embedded within the flow. One of the characteristics of the duct flow is the presence of secondary flows perpendicular to the mean longitudinal flow whose intensity is weak compared with the latter (1–2% of the bulk velocity). The LES, which are performed at a significantly reduced cost compared with the DNS, perfectly reproduce the intensity of these weak secondary flows. Note that statistical one-point closure models have to be elaborated to achieve such a good statistical description. We have performed a detailed investigation of the flow anisotropy which reveals that, near the duct central plane, the flow anisotropy is qualitatively similar to the classical turbulent channel flow or the turbulent boundary layer with periodicity along the spanwise direction. Away from this central plane, we have investigated in detail how the flow anisotropy is modified by the presence of the lateral wall.

When the asymmetrical heating is applied, significant modifications of the flow characteristics have been observed. The secondary flows located near the heated wall are enhanced both in size and intensity. The increase of the viscosity near the heated wall plays a major rôle. Near the heated wall, the turbulence was strongly reduced due to the enhanced viscosity effects in this flow region. The viscous thickness near the heated wall was found to be significantly enhanced compared with the heated case. All the characteristic structures of the classical boundary layer, such as the low- and high-speed streaks, the associated ejections and the associated quasi-longitudinal vortices are observed in both the non-heated and the heated ducts. These flow structures seem to be similar in nature and origin for both the non-heated case and the heated case. Indeed, although a slight increase is noticed when heating is applied, the spanwise wavelength of the streaks remains close to the classical value of ≈ 100 viscous units for most of the investigated cases. Associated with the low-speed streaks, strong ejections take place: the maximum of the ejection activity occurs around $y^+ \approx 40$ as indicated by the minimum in the second quadrant of the $\langle u'v' \rangle$ component of the Reynolds stress.

Since the heating yields an augmentation of the viscous thickness, the size of the turbulent structures (streaks, ejections) is actually significantly larger with increased heating compared with the duct characteristic size such as its hydraulic diameter. Consequently, for the strongest heating we have applied, a saturation of the spanwise wavelength of the low- and high-speed streak system is observed near the heated wall due to the limitation imposed by the duct width. For strong enough heating, only one meandering low-speed streak may appear near the duct central plane corresponding to slow and hot fluid ejected from the wall. The latter is surrounded by two high-speed streaks corresponding to fast and cold fluid impinging on the wall. The violent ejections associated with the central low-speed streak induce a lifting of the vortex lines from the heated wall and their subsequent stretching gives rise to quasi-longitudinal vorticity structures corresponding to the aligned legs of consecutive hairpin shaped vortex lines. The longitudinal vorticity generated by this stretching mechanism, when expressed in wall-units, is found to be larger in the heated duct: this can be attributed to the enhanced size of the ejections which extend further away from the wall in a region of faster fluid inducing a stronger longitudinal vorticity generation by stretching.

Finally, a conditional statistical sampling of the strongest ejection events has allowed us to investigate in detail the effects due to compressibility. We have shown that the ejection process is amplified by the important fluid expansion taking place at the bottom of the ejection: this is a consequence of the secondary flow associated with the strong ejection which generates a convergence of the cold fluid from the duct interior towards the hot wall where it expands.

This research was supported by the Centre National d'Etudes Spatiales (CNES, France). Computations were carried out at the Institut du Développement et des Ressources en Informatique Scientifique (IDRIS, France). First author acknowledges the Universidad Nacional Autónoma de México (UNAM, Mexico) and Secretaria de Educación Pública de México (SEP, Mexico) for financial support.

REFERENCES

Antonia, R. A., Danh, H. Q. & Prabhu, A. 1977 Response of turbulent boundary layer to a step change heat flux. *J. Fluid Mech.* **99**, 153–177.

Antonia, R. A., Kim, J. & Browne, W. B. 1991 Some characteristics of small-scale in a turbulent duct flow. *J. Fluid Mech.* **233**, 369–388.

Brundett, E. & Baines, W. D. 1964 The production and diffusion of vorticity in duct flow. *J. Fluid Mech.* **19**, 375–394.

Cheng, R. K. & Ng, T. T. 1982 Some aspects of strongly turbulent boundary layer flow. *Phys. Fluids* **25**, 1333–1341.

Cheng, R. K. & Ng, T. T. 1996 Conditional Reynolds stress in a strong heated turbulent boundary layer with premixed combustion. *Phys. Fluids* **28**, 433–488.

Coleman, G. N., Kim, J. & Moser, R. D. 1995 A numerical study of turbulent supersonic isothermal-wall channel flow. *J. Fluid Mech.* **305**, 159–183.

Comte, P. 1993 Numerical methods for compressible flows. *Les Houches, session LVIX*. Elsevier.

Comte, P. & Lesieur, M. 1997 Large-eddy simulation of compressible turbulent flows. *Turbulence in Compressible Flows, AGARD/VKI Course, AGARD Rep.* 819.

David, E. 1993 Modélisation des écoulements compressibles et hypersoniques: Une approche instationnaire. PhD Thesis, Institut National Polytechnique de Grenoble, France.

Delcayre, F. 1999 Étude par simulation des grandes échelles d'un écoulement décollé: la marche descendante. PhD Thesis, Institut National Polytechnique de Grenoble, France.

Demuren, A. & Rodi, W. 1984 Calculation of turbulence-driven secondary motion in non circular ducts. *J. Fluid Mech.* **140**, 189–222.

Dubief, Y. & Delcayre, F. 2000 On coherent-vortex identification in turbulence. *J. Turbulence* **1**, 001.

Ducros, F., Comte, P. & Lesieur, M. 1996 Large-eddy simulation of transition to turbulence in a boundary-layer developing spatially over a flat plate. *J. Fluid Mech.* **326**, 1–36.

Eibeck, P. A. & Eaton, J. K. 1987 Heat transfer effects of a longitudinal vortex embedded in a turbulent boundary layer. *J. Heat Transfer* **109**, 16–24.

Favre, A. 1965 Equations des gaz turbulents compressibles, II: Méthode des vitesses macroscopiques pondérées par la masse volumique. *J. Méc.* **4**, 391–421.

Fletcher, C. A. J. 1988 *Computational Techniques for Fluid Dynamics* 2. Springer.

Gavrilakis, S. 1992 Numerical simulation of low Reynolds number turbulent flow through a straight square duct. *J. Fluid Mech.* **244**, 101–12.

Gessner, F. B. 1983 The origin of secondary flow in turbulent flow along a corner. *J. Fluid Mech.* **58**, 1–23.

Gessner, F. B. & Jones, J. B. 1965 On some aspects of fully developed turbulent flow in a rectangular channel. *J. Fluid Mech.* **23**, 689–713.

Gottlieb, D. & Turkel, E. 1976 Dissipative two four methods for time-dependent problems. *Math. Comput*. **30**, 703–723.

Hunt, J., Wray, A. & Moin, P. 1988 Eddies, stream, and convergence zones in turbulent flows. *Center for Turbulence Research Rep.* CTR-S88.

Huser, A. & Biringen, S. 1993 Direct numerical simulation of turbulent flow in a square duct. *J. Fluid Mech.* **257**, 65–95.

Jones, O. C. 1976 An improvement in the calculation of turbulent friction in rectangular ducts. *Trans. ASME: J. Fluids Engng* **98**, 173–181.

Knight, D. & Patel, H. 1985 Boundary shear stress distribution in rectangular duct flow. *Turbulence Measurements and Flow Modeling* (ed. C. J. Chen), pp. 707–711. Hemisphere.

Lamballais, E., Lesieur, M. & Métais, O. 1997 Probability distribution functions and coherent structures in a turbulent channel. *Phys. Rev.* E **56**, 6761–6766.

Le, H., Moin, P. & Kim, J. 1997 Direct numerical simulation of turbulent flow over a backward-facing step. *J. Fluid Mech.* **330**, 349–374.

Lumley, J. L. & Newman, G. W. 1977 The return to isotropy of homogeneous turbulence. *J. Fluid Mech.* **82**, 161–178.

Madabhushi, R. & Vanka, S. 1991 Large eddy simulation of turbulent-driven secondary flow square duct. *Phys. Fluids* A **3**, 2734–2745.

Métais, O. & Lesieur, M. 1992 Spectral large-eddy simulation of isotropic and stably-stratified turbulence. *J. Fluid Mech.* **239**, 157–194.

Métais, O. & Lesieur, M. 1996 New trends in large eddy simulations of turbulence. *Annu. Rev. Fluid Mech.* **28**, 45–82.

Robinson, S. 1991 Coherent motions in the turbulent boundary layer. *Annu. Rev. Fluid Mech.* A **23**, 601–639.

Salinas-Vázquez, M. 1999 Simulation numérique des grandes échelles d'écoulements dans les canaux de refroidissement de moteur fusée. PhD Thesis, Institut National Polytechnique de Grenoble, France.

Salinas-Vázquez, M. & Métais, O. 1999 Large eddy simulation of a square duct with heat flow. *Direct and Large-Eddy Simulation III* (ed. P. R. Voke, N. D. Sandham & L. Kleiser), pp. 13–24. Kluwer.

Schlichting, H. 1979 *Boundary-Layer Theory*. McGraw-Hill.

Wang, W. & Pletcher, R. H. 1996 On the large eddy simulation of a turbulent channel flow with significant heat transfer. *Phys. Fluids* **8**, 3354–3365.

Wardana, I. N. G., Ueda, T. & Mizomoto, T. 1994 Effect of strong wall heating on turbulence statistics of a channel flow. *Exps. Fluids* **18**, 87–94.

Wardana, I. N. G., Ueda, T. & Mizomoto, T. 1995 Velocity-temperature correlations in a strongly heated channel flow. *Exps. Fluids* **18**, 454–461.

White, F. M. 1991 *Viscous Fluid Flow*. McGraw-Hill.

Willmarth, W. W. & Lou, S. S. 1972 Structure of the Reynolds stress near the wall. *J. Fluid Mech.* **55**, 65–92.